

Transient Corotating Clumps Around Adolescent Low-Mass Stars From Four Years of TESS

2 LUKE G. BOUMA,^{1,*} RAHUL JAYARAMAN,² SAUL RAPPAPORT,² LUISA M. REBULL,¹ LYNNE A. HILLENBRAND,¹ JOSHUA N. WINN,³
3 ALEXANDRE DAVID-URAZ,^{4,5} AND GÁSPAR Á. BAKOS³

4 ¹Department of Astronomy, MC 249-17, California Institute of Technology, Pasadena, CA 91125, USA

5 ²MIT Kavli Institute and Department of Physics, 77 Massachusetts Avenue, Cambridge, MA 02139

6 ³Department of Astrophysical Sciences, Princeton University, 4 Ivy Lane, Princeton, NJ 08540, USA

7 ⁴Department of Physics and Astronomy, Howard University, Washington DC, 20059

8 ⁵Center for Research and Exploration in Space Science and Technology, and X-ray Astrophysics Laboratory, NASA/GSFC, Greenbelt, MD 20771, USA

9 (Received 2023 September 8; Revised —; Accepted —)

ABSTRACT

11 Complex periodic variables (CPVs) are stars that exhibit highly structured and periodic optical light curves.
12 Previous studies have indicated that these stars are typically disk-free pre-main-sequence M dwarfs with rotation
13 periods ranging from 0.2 to 2 days. To advance our understanding of these enigmatic objects, we conducted
14 a blind search using TESS 2-minute data of 65,760 K and M dwarfs with $T < 16$ and $d < 150$ pc. We found
15 50 high-quality CPVs, and subsequently determined that most are members of stellar associations. Among
16 the new discoveries are the brightest ($T \approx 9.5$), closest ($d \approx 20$ pc), and oldest (≈ 200 Myr) CPVs known. One
17 exceptional object, LP 12-502, exhibited up to eight flux dips per cycle. Some of these dips coexisted with
18 slightly different periods, and the shortest-duration dips precisely matched the expected timescale for transiting
19 small bodies at the corotation radius. Broadly, our search confirms that CPVs are mostly young ($\lesssim 150$ Myr) and
20 low-mass ($\lesssim 0.4 M_{\odot}$). The flux dips characteristic of the class have lifetimes of ≈ 100 cycles, although stellar
21 flares seem to induce sudden dip collapse once every few months. The most plausible explanation for these
22 phenomena remains corotating concentrations of gas or dust. The gas or dust is probably entrained by the star's
23 magnetic field, and the sharp features could result from a multipolar field topology, a hypothesis supported by
24 correspondences between the light curves of CPVs and of rapidly rotating B stars known to have multipolar
25 magnetic fields.

26 **Keywords:** Weak-line T Tauri stars (1795), Periodic variable stars (1213), Circumstellar matter (241), Star
27 clusters (1567), Stellar magnetic fields (1610), Stellar rotation (1629)

1. INTRODUCTION

29 All young stars vary in optical brightness, and the origin of
30 such variability is, in most cases, understood. Well-explored
31 sources of optical variability include inhomogeneities on
32 stellar surfaces such as starspots and faculae (e.g. Basri
33 2021), occultations by circumstellar disks (e.g. Bodman
34 et al. 2017), and, in geometrically favorable circumstances,
35 eclipses by stars and planets (e.g. Rizzuto et al. 2020). More
36 exotic sources of optical variability that are potentially rel-
37 evant to this work include transiting exocomets (e.g. β Pic;
38 Zieba et al. 2019), disintegrating rocky bodies (e.g. KOI-
39 2700; Rappaport et al. 2014), and occultations by circum-
40 stellar plasma clumps (e.g. σ Ori E; Townsend et al. 2005;
41 Townsend & Owocki 2005).

Corresponding author: Luke G. Bouma
luke@astro.caltech.edu

* 51 Pegasi b Fellow

42 Data from K2 (Howell et al. 2014) and TESS (Ricker et al.
43 2015) have revealed a new class of variable star for which the
44 root cause of variability is only beginning to become clear:
45 complex periodic variables (CPVs). These objects are iden-
46 tified from their optical light curves, which show nearly pe-
47 riodic troughs that are either sharp or broad; these troughs
48 are often superposed on quasi-sinusoidal spot-like modula-
49 tion (Stauffer et al. 2017, 2018b; Zhan et al. 2019). Some
50 CPVs show up to eight dips per cycle. Most CPVs are pre-
51 main-sequence M dwarfs with ages of ≈ 5 –150 million years
52 (Myr), and rotation periods of 0.2–2 days. They are observed
53 to comprise ≈ 1 –3% of M dwarfs younger than 100 Myr (Re-
54 bull et al. 2016; Günther et al. 2022). They generally do not
55 show near-infrared excesses indicative of dusty disks, but the
56 wavelength-dependent dip amplitudes of some CPVs is con-
57 sistent with reddening by dust (Onitsuka et al. 2017; Bouma
58 et al. 2020; Günther et al. 2022; Koen 2023). The dip ampli-
59 tudes and phases usually evolve gradually over tens to hun-
60 dreds of cycles, although they have occasionally been ob-

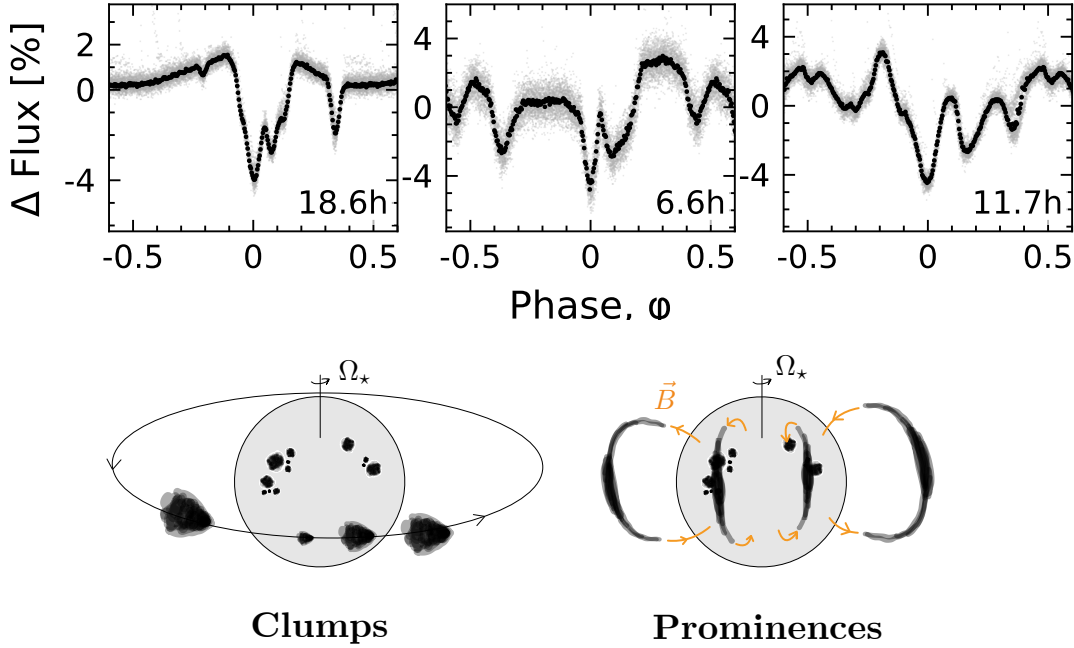


Figure 1. Complex periodic variables (CPVs): *Top:* Phase-folded TESS light curves for three CPVs. Each panel shows the average of the data accumulated over one month, relative to the mean stellar brightness. Gray circles are raw 2-minute data; black circles are binned to 300 points per cycle. The period in hours is printed in the bottom right corner. Left-to-right, the objects are LP 12-502 (TIC 402980664; Sector 19), TIC 94088626 (Sector 10), and TIC 425933644 (Sector 28). *Bottom:* Cartoon configurations for magnetically-entrained corotating material. The dust clump scenario (left) and gas prominence scenario (right) propose different opacity sources, and different occultation geometries.

served to change abruptly within one cycle (e.g. Stauffer et al. 2017; Palumbo et al. 2022; Popinchalk et al. 2023).

The sharp features of CPV light curves can have durations as short as 5% of the rotation period (P_{rot}), which is too short to be caused by starspots rotating into and out of view. Starspots produce flux variations with characteristic timescales of P_{rot} and $0.5P_{\text{rot}}$. With finely-tuned viewing geometries, starspots can produce dip durations as short as $\approx 0.2P_{\text{rot}}$, but in such cases, limb darkening causes the dip amplitudes to be smaller than the observed amplitudes of $\sim 1\%$ (see Stauffer et al. 2017, Figures 37-41). Thus, a “starspot-only” scenario can be ruled out for many CPVs (Stauffer et al. 2017; Zhan et al. 2019; Koen 2021). Given that many CPVs cannot be explained by starspots alone, and working under the assumption that all CPVs share the same basic physical scenario, we discard the “starspot-only” model. Instead, the correct explanation probably involves spatially concentrated circumstellar material (e.g. Stauffer et al. 2017; Günther et al. 2022).

Figure 1 illustrates two proposed configurations for the extrinsic material. The first scenario invokes opaque dust “clumps” that orbit near the Keplerian corotation radius [$R_c = (GM/\Omega^2)^{1/3}$, where $\Omega = 2\pi/P_{\text{rot}}$] and periodically transit the star (e.g. Stauffer et al. 2017; Farihi et al. 2017; Sanderson et al. 2023). The second scenario invokes “prominences”, long-lived condensations of cool, dense, marginally-ionized gas that are embedded within the hotter corona and that corotate with the star (Collier Cameron & Robinson 1989; Jardine

& Collier Cameron 2019; Waugh & Jardine 2022). These hypothetical prominences are analogous to quiescent prominences and filaments seen in the solar corona (see e.g. Vial & Engvold 2015), though rather than existing at a fraction of the stellar radius as in the solar case, they would exist at distances of a few stellar radii. A final possibility is that an optically-thick ring obscures a narrow band of the stellar photosphere (Zhan et al. 2019); hot spots passing behind such a ring could produce sudden dips. We disfavor this scenario for reasons described in Appendix A.

While the dust clump and gas prominence hypotheses both invoke magnetically-entrained material, the two pictures differ in the origin and the composition of the occulting material. “Dust clumps” invoke opacity from dust, which would need to be collisionally charged (Sanderson et al. 2023), and which might be sourced from a low-mass debris disk. “Gas prominences” invoke opacity from partially-ionized gas, perhaps bound-free transitions in hydrogen or a molecular opacity. The gas might be sourced from a stellar wind. Unambiguous evidence in support of either scenario has yet to be acquired. Such evidence might include a spectroscopic detection of silicate $10\ \mu\text{m}$ dust absorption during a dip, or perhaps detection of transient Balmer-line excesses as a function of cycle phase, similar to observations made in systems such as AB Dor (see Collier Cameron 1999) or PTFO 8-8695 (Johns-Krull et al. 2016).

In both models, the corotation radius is the location at which matter concentrates. The empirical basis for this is that

the sharp CPV features are superposed over smooth, quasi-sinusoidal starspot profiles. The theoretical importance of the corotation radius has been noted in previous studies of magnetic rotators (e.g. Lamb et al. 1973; Nakajima 1985; Königl 1991; Long et al. 2005). In regions where the magnetic field dominates the flow (i.e. $B^2/8\pi > \rho v^2/2$), matter is dragged along with the field lines. Within such regions, charged gas or dust can become trapped at corotation because of the four relevant forces – gravity, Lorentz, inertial Coriolis, and inertial centrifugal – the Lorentz and Coriolis only act perpendicular to field lines, while gravity and the centrifugal force are in balance at R_c (e.g. Townsend & Owocki 2005, their Section 2). Another way to phrase this statement is that, in the corotating frame, the effective potential experienced by charged particles tends to have local minima at R_c ; given a flow from either the star or from a tenuous accretion disk, this local potential minimum enables material to build up (Townsend & Owocki 2005).

While theoretical heritage for understanding magnetic rotators exists, CPVs have remained mysterious because they have been both hard to discover and hard to characterize. They have been hard to discover because they are rare: CPVs comprise $\approx 1\%$ of the youngest $\approx 1\%$ of M dwarfs (Rebull et al. 2018). Out of the millions of stars monitored by K2 and TESS, about 70 CPVs have been reported to date (Rebull et al. 2016; Stauffer et al. 2017, 2018b; Zhan et al. 2019; Bouma et al. 2020; Stauffer et al. 2021; Günther et al. 2022; Popinchalk et al. 2023). They have been hard to characterize because many of the known CPVs are faint; the initial K2 discoveries (Rebull et al. 2016; Stauffer et al. 2017) were M2–M6 dwarfs at distances $\gtrsim 100$ pc, with optical brightnesses of $V \approx 15.5$ to $V > 20$. At such magnitudes, high-resolution time-series spectroscopy is out of reach with current facilities, despite the potential utility of such observations.

In this work, we aim to find bright and nearby CPVs, since these objects will be the most amenable to detailed photometric and spectroscopic analyses. To do this, we use 2-minute cadence data acquired by TESS between 2018 July and 2022 September (Sectors 1–55; Cycles 1–4). We present our search methods in Section 2, and the resulting CPV catalog in Section 3. The observed evolution of many CPVs over a two-year baseline is described in Section 4, including a deep-dive into the behavior of an especially interesting object, LP 12–502. We discuss a few implications in Section 5, and conclude in Section 6.

Some comments on nomenclature are needed. What we are calling “complex periodic variables” (Koen 2023) have also been called “complex rotators” (Zhan et al. 2019; Günther et al. 2022; Popinchalk et al. 2023), “transient flux dips”, “persistent flux dips”, and “scallop shells” (Stauffer et al. 2017). The CPVs should not be conflated with “dippers”, which are classical T Tauri stars with infrared excesses, and which show large-amplitude variability linked to obscuring inner disk structures and accretion hot spots (Cody et al. 2014; Robinson et al. 2021). The phenomenology and stellar properties of CPVs and dippers are quite different (though see Sections 3.3 and 5.9). The defining phenomenological

features of the CPVs are that their light curves are *complex*, relative to quasi-sinusoidal starspots, and the complex features are *periodic*, meaning they typically repeat for at least tens of days. While rotation likely does play a central role in explaining their physical behavior, the acronym for “complex rotator” is already used in the astrophysical literature for cosmic rays. Given these considerations, we refer to the stars as complex periodic variables (CPVs); our preferred explanation for their behavior is that transient clumps of gas or dust orbit at their corotation radii.

2. METHODS

2.1. Stellar selection function

We searched for CPVs by analyzing the short-cadence data acquired by TESS between 2018 July 25 and 2022 September 1 (Sectors 1–55). Specifically, we used the 2-minute cadence light curves produced by the Science Processing and Operations Center at the NASA Ames Research Center (Jenkins et al. 2016). While the TESS data products from these sectors also included full frame images with cadences of 10 and 30 minutes for a larger number of sources, we restricted our attention to the 2-minute data for the sake of uniformity and simplicity in data handling. In exchange, we sacrificed both completeness and homogeneity of the selection function. While TESS cumulatively observed $\approx 90\%$ of the sky for at least one lunar month between 2018 July and 2022 September, the 2-minute cadence data were collected for only a subset of observable stars that were preferentially nearby and bright (see Fausnaugh et al. 2021). The total 2-minute data volume from Sectors 1–55 included 1,087,475 short-cadence light curves, which were available for 428,121 unique stars.

To simplify our search, we defined our target sample as stars with 2-minute cadence TESS light curves satisfying the following four conditions:

$$T < 16 \quad (\text{Amenable with TESS}) \quad (1)$$

$$G_{\text{BP}} - G_{\text{RP}} > 1.5 \quad (\text{Red stars only}) \quad (2)$$

$$M_G > 4 \quad (\text{Dwarf stars only}) \quad (3)$$

$$d < 150 \text{ pc} \quad (\text{Close stars only}). \quad (4)$$

Here, $M_G = G + 5 \log(\varpi_{\text{as}}) + 5$ is the Gaia G -band absolute magnitude, ϖ_{as} is the parallax in units of arcseconds, and d is a geometric distance defined by inverting the parallax and ignoring any zero-point correction. We performed this selection by cross-matching TIC8.2 (Stassun et al. 2019; Paegert et al. 2021) against the Gaia DR2 point-source catalog (Gaia Collaboration et al. 2018). We opted for Gaia DR2 rather than DR3 because the base catalog for TIC8 was Gaia DR2, which facilitated a one-to-one crossmatch using the Gaia source identifiers. The target sample ultimately included 65,760 M dwarfs and late-K dwarfs, down to $T < 16$ and out to $d < 150$ pc. For stars with multiple sectors of TESS data available, we searched for CPV signals independently. In total, our 65,760 star target list included 180,017 month-long light curves.

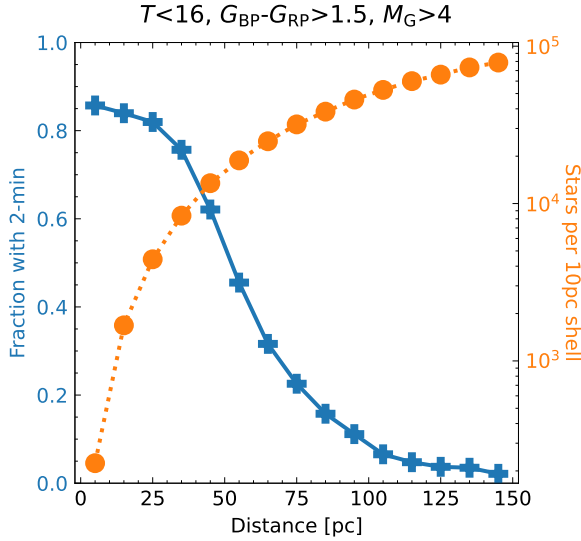


Figure 2. Completeness of the TESS 2-minute data for late-K and early M dwarfs near the Sun, from Sectors 1-55. The orange dotted curve shows the number of stars in successive radial shells, each with a width of 10pc. To be part of our selection function, these stars must meet the following conditions: they must be red dwarf stars ($G_{\text{BP}} - G_{\text{RP}} > 1.5$; $M_G > 4$) amenable for TESS observations ($T < 16$). The blue solid curve shows the fraction of such stars with at least one sector of TESS 2-minute cadence data acquired between Sectors 1-55.

We assessed the completeness of our selection function by comparing the number of stars with TESS Sector 1-55 short-cadence data against the number of Gaia DR2 point sources. We required all stars to meet conditions 1–4. The results are shown in Figure 2. TESS 2-minute data exist for $\approx 50\%$ of $T < 16$ M and late-K dwarfs at ≈ 50 pc. Within 20 pc, $\gtrsim 80\%$ of the $T < 16$ M and late-K dwarfs have at least one sector of short-cadence data. Beyond 100 pc, $\lesssim 10\%$ of such stars have any short-cadence data available. This can be translated into our sensitivity for the lowest mass stars by considering that the spectral type of a $T = 16$ star at $d = 50$ pc is $\approx \text{M}5.5\text{V}$, corresponding to a main-sequence mass of $\approx 0.12 M_\odot$.

2.2. CPV discovery

Prior to this study, most CPVs have been found by visually examining all the light curves of stars in young clusters (Rebull et al. 2016; Stauffer et al. 2017; Popinchalk et al. 2023), or by flagging light curves with short periods and strong Fourier harmonics for visual inspection (Zhan et al. 2019). In this work, we implemented a new search approach based on counting the number of sharp local minima in phase-folded light curves, while also using the Fourier approach. We applied these two search techniques independently to our 65,760 targets.

2.2.1. Counting dips

The dip counting technique aims to count sharp local minima in phase-folded light curves. The most remarkable CPVs

often show three or more dips per cycle, which distinguishes them from other types of variables such as synchronized and spotted binaries (RS CVn stars).

For our dip-counting pipeline, we began with the PDC_SAP light curves for each sector (Smith et al. 2017), removed non-zero quality flags, and normalized the light curve by dividing out its median value. We then flattened the light curve using a 5-day sliding median filter, as implemented in wotan (Hipke et al. 2019). We computed a periodogram of the resulting cleaned and flattened light curve, opting for the Stellingwerf (1978) phase dispersion minimization (PDM) algorithm implemented in astrobase (Bhatti et al. 2021) due to its shape agnosticism. If a period P below 2 days was identified, we reran the periodogram at a finer grid to improve the accuracy of the period determination.

Once a star’s period was identified, we binned the phased light curve to 100 points per cycle. To separate sharp local minima from smooth spot-induced variability, we then iteratively fit robust penalized splines to the wrapped phase-folded light curve, excluding points more than two standard deviations away from the local continuum (Hipke et al. 2019). The wrapping procedure is discussed below. In this fitting framework, the maximum number of equidistant spline knots per cycle is the parameter that controlled the meaning of “sharp” — we allowed at most 10 such knots per cycle, though for most stars fewer knots were preferred based on cross-validation using an ℓ^2 -norm penalty. An example fit is shown in panel (e) of Figure 3.

We then identified local minima in the resulting residual light curve using the SciPy find_peaks utility (Virtanen et al. 2020), which is based on comparing adjacent values in an array. For a peak to be flagged as significant, we required it to have a width of at least $0.02P$, and a height of at least twice the noise level. The noise level was defined as the 68th percentile of the distribution of the residuals from the median value of $\delta f_i \equiv f_i - f_{i+1}$, where f is the flux and i is an index over time. In panel (e) of Figure 3, automatically-identified local minima are shown with the gray triangles.

Wrapping is necessary to eliminate edge effects when fitting the light curve and when identifying local minima in the residuals. A phased light curve would usually cover phases $\phi \in [0, 1]$. We instead performed the analysis described above using a phase-folded light curve spanning $\phi \in [-1, 2]$, which was created by duplicating and concatenating the ordinary phase-folded light curve. The free parameters we adopted throughout the analysis – for instance the maximum number of spline knots per cycle, and the height and depth criteria for dips – were chosen during testing based on the desire to correctly re-identify a large fraction ($> 90\%$) of previously known CPVs, while also being able to consistently reject common false positives such as spot-induced variability and eclipsing binaries.

In short, CPV candidates were identified by requiring a peak PDM period below two days and the presence of at least three sharp local minima, based on at least one sector of the TESS 2-minute data. Candidates were then inspected visually as described in Section 2.2.3.

303 2.2.2. Fourier analysis

304 We performed an independent search using a Fourier-based
 305 approach, following Zhan et al. (2019) and Pribulla et al.
 306 (2023, their Section 1.3). Starting with the PDC_SAP light
 307 curves, we normalized each light curve, and then re-binned
 308 it into equal width 2-minute bins to account for the uneven
 309 spacing in the TESS data, as well as the data gap caused
 310 by satellite downlink during each sector. We then padded
 311 the data to ensure that the light curve had a length that was
 312 a power of two, as described by Zhan et al.. After tak-
 313 ing the Fourier transform of the padded light curve using
 314 numpy.fft, we searched for peaks with a significance ex-
 315 ceeding 12σ within a set of 500 frequency bins.

316 Peaks of significance were found for $\approx 10\%$ of the searched
 317 stars. For all such cases, we generated an interim “summary
 318 sheet” with information about the star, its full and folded light
 319 curves, Fourier transform, potential contaminating stars, and
 320 information about these contaminating stars. We then re-
 321 viewed each summary sheet, and tentatively classified each
 322 light curve based on visual inspection of its morphology
 323 (with common categories including eclipsing binary, CPV,
 324 RS CVn, and cataclysmic variable).

325 2.2.3. Manual vetting

326 We homogeneously assessed whether the objects identi-
 327 fied using the dip-counting (Section 2.2.1) and Fourier (Sec-
 328 tion 2.2.2) approaches were consistent with expectations for
 329 CPVs by assembling the data shown in Figure 3. We labeled
 330 a star as a “good” CPV if it met all of the following criteria
 331 for at least one TESS sector:

- 332 • $P < 2$ days.
- 333 • At least three dips per cycle, or else otherwise oddly-
 334 shaped dips relative to expectations for quasi-sinusoidal
 335 starspot-induced modulation.
- 336 • Persistent dips over multiple consecutive rotation cycles.

337 We also noted “possible” CPVs for which the classifica-
 338 tion was more ambiguous, and “false positives” that are definitely
 339 not CPVs. The most common false positives for both the
 340 Fourier and dip-counting techniques were eclipsing binaries,
 341 ordinary spotted rapid rotators, and light curves that were
 342 complex due to multiple stars contributing to the photomet-
 343 ric aperture. Our specialized dip-counting pipeline flagged
 344 368 unique stars for visual inspection; about 20% were sub-
 345 sequently labeled either good or possible CPVs. From the
 346 more general Fourier pipeline, $\approx 0.5\%$ of stars that passed
 347 the 12σ peak threshold were eventually classified as CPVs.

348 2.3. Stellar properties

349 2.3.1. Ages

350 While most of our target stars were field stars, color-
 351 absolute magnitude diagrams suggested that most CPVs
 352 tended to be on the pre-main-sequence (e.g. panel (k) of Fig-
 353 ure 3). We therefore estimated stellar ages by checking for
 354 probabilistic spatial and kinematic associations between the
 355 CPVs and known clusters in the solar neighborhood. For

356 most stars in our sample, we did this using BANYAN Σ
 357 (Gagné et al. 2018).¹ This algorithm calculates the proba-
 358 bility that a given star belongs to either the field, or to any of
 359 27 young clusters (“associations”) within 150 pc of the Sun.
 360 This is achieved by modeling the field and cluster popula-
 361 tions as multivariate Gaussian distributions in 3-D position
 362 and 3-D velocity space. We used the Gaia DR2 sky positions,
 363 proper motions, and distances to calculate the membership
 364 probabilities. BANYAN Σ in turn analytically marginalizes
 365 over the radial velocity dimension. The probabilities returned
 366 by this procedure are qualitatively helpful, but should be in-
 367 terpreted with caution because the assumption of Gaussian
 368 distributions is questionable for most groups within the solar
 369 neighborhood (see e.g. Kerr et al. 2021, Figure 10).

370 For a few cases where BANYAN Σ yielded ambiguous re-
 371 sults, we consulted the meta-catalog of young, age-dated, and
 372 age-dateable stars provided by Bouma et al. (2022), and also
 373 searched the local volume around each star for co-moving
 374 companions.² Finally, to provide a base for comparison, we
 375 also ran the BANYAN Σ membership analysis on our entire
 376 65,760 target star sample.

377 2.3.2. Effective temperatures, radii, and masses

378 We determined the stellar effective temperature and radii
 379 for the CPVs by fitting the broadband spectral energy distri-
 380 butions (SEDs); we then estimated the masses by interpolat-
 381 ing against the sizes, temperatures, and ages of the PARSEC
 382 v1.2S models (Bressan et al. 2012; Chen et al. 2014).

383 For the SED fitting, we used astroARIADNE (Vines &
 Jenkins 2022). We adopted the BT-Settl stellar atmosphere
 384 models (Allard et al. 2012) assuming the Asplund et al.
 385 (2009) solar abundances, and the Barber et al. (2006) water
 386 line lists. The broadband magnitudes we considered included
 387 $GG_{BP}G_{RP}$ from Gaia DR2, $Vgri$ from APASS, JHK_S from
 388 2MASS, SDSS riz , and the WISE $W1$ and $W2$ passbands.
 389 We omitted UV flux measurements from our SED fit to avoid
 390 any possible bias induced by chromospheric UV excess. We
 391 omitted WISE bands $W3$ and $W4$ due to reliability con-
 392 cerns. astroARIADNE compares the measured broadband
 393 flux measurements against pre-computed model grids, and by
 394 default fits for six parameters: $\{T_{\text{eff}}, R_*, A_V, \log g, [\text{Fe}/\text{H}], d\}$.
 395 The distance prior is drawn from Bailer-Jones et al. (2021).
 396 The surface gravity and metallicity are generally uncon-
 397 strained. Given our selection criteria for the stars, we as-
 398 sumed the following priors for the temperature, stellar size,
 399 and extinction:

$$399 T_{\text{eff}}/\text{K} \sim \mathcal{N}(3000, 1000), \quad (5)$$

$$400 R_*/R_\odot \sim \mathcal{T}_N(0.5, 0.3, 0.1, 1.5), \quad (6)$$

$$401 A_V/\text{mag} \sim \mathcal{U}(0, 0.2), \quad (7)$$

402 for \mathcal{N} the Gaussian and \mathcal{U} the uniform distributions, and
 403 $\mathcal{T}_N(\mu, \sigma, a, b)$ a truncated normal distribution with mean μ ,

¹ https://github.com/jgagneastro/banyan_sigma, git commit 394b486

² <https://github.com/adamkraus/Comove>, git commit 278b372

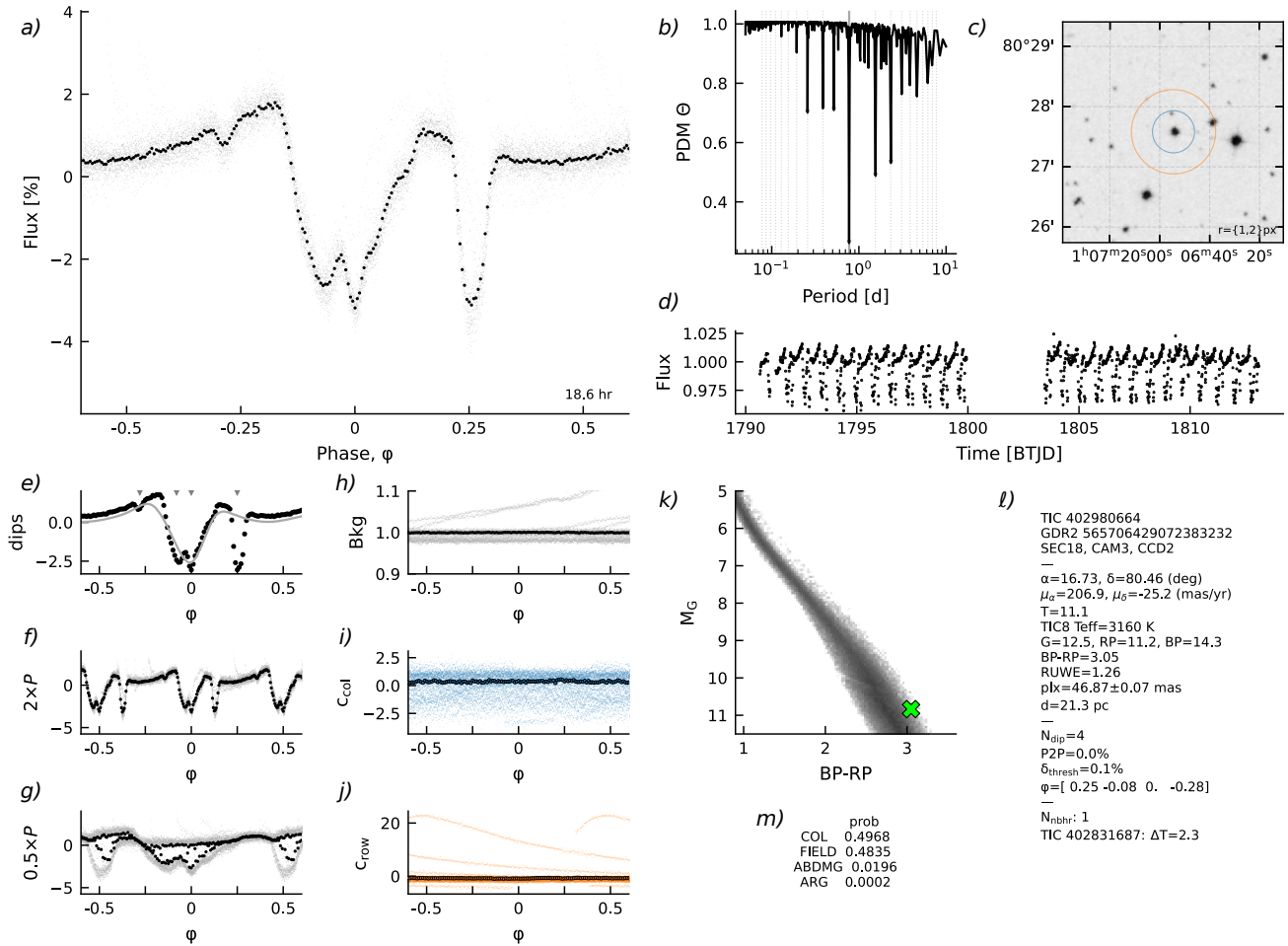


Figure 3. Validation plots used to classify CPVs. The complete figure set contains one image per sector for each of the 66 objects in Table 1, and is accessible both through the online journal and via <https://zenodo.org/record/8327508>. Panels are as follows. *a*): Phase-folded light curve; gray points are raw 2-minute data and black points are binned to 200 points per cycle. The adopted period is given in the lower-right corner. *b*): Phase-dispersion minimization (PDM) periodogram. Dotted lines show up to the 10th harmonic and subharmonic. *c*): DSS finder chart, with 21'' and 42'' radius circles for scale. One TESS pixel has a full side length of 21''. *d*): Cleaned light curve, binned to 20-minute cadence, in Barycentric TESS Julian Date (BTJD). *e*): Phase-folded light curve, binned to 100 points per cycle. The gray line denotes the spline-fit to the wrapped phase-folded light curve, and small gray triangles denote automatically identified local minima. *f*): Phase-folded light curve at twice the peak period. *g*): Phase-folded light curve at half the peak period. *h*): Phase-folded time-series within the “background” aperture defined in the SPOC light curves. *i*): Phase-folded flux-weighted centroid in the column direction. *j*): Phase-folded flux-weighted centroid in the row direction. *k*): Gaia DR2 color–absolute magnitude diagram. The gray background denotes stars within 100 pc from [Gaia Collaboration et al. \(2021\)](#). *l*): Information from Gaia DR2, TIC8, and the automated dip-counting search pipeline. “Neighbors”, abbreviated “nbhr”, are listed within apparent distances of 2 TESS pixels if $\Delta T < 2.5$. *m*): BANYAN Σ v1.2 association probabilities, calculated using positions, proper motions, and the parallax.

standard deviation σ , and lower and upper bounds a and b . We validated our chosen upper bound on A_V using a 2MASS color-color diagram. Finally, using Dynesty (Speagle 2020), we sampled the posterior probability assuming the default Gaussian likelihood, and set a stopping threshold of $d\log \mathcal{Z} < 0.01$, where \mathcal{Z} denotes the evidence.

With the effective temperatures and stellar radii from the SED fit, we estimated the stellar masses by interpolating against the PARSEC isochrones (v1.2S Chen et al. 2014). The need for models that incorporate some form of correction

for young, active M dwarfs is well-documented (e.g. Stassun et al. 2012; David & Hillenbrand 2015; Feiden 2016; Somers et al. 2020). Plausible explanations for the disagreement between observed and theoretical M dwarf colors and sizes include starspot coverage (e.g. Gully-Santiago et al. 2017) and potentially incomplete line lists (e.g. Rajpurohit et al. 2013). In the PARSEC models, Chen et al. (2014) performed an empirical correction to the temperature–opacity relation drawn from the BT-Settl model atmospheres, in order to match observed masses and radii of young eclipsing binaries. This is

sufficient for our goal of estimating stellar masses. Given our estimates of $\{\tilde{T}_{\text{eff}}, \tilde{M}_*, \tilde{t}\}$, and approximating their uncertainties as Gaussian $\sigma_{\tilde{T}_{\text{eff}}}$, $\sigma_{\tilde{M}_*}$ and $\sigma_{\tilde{t}}$, we define a distance metric Δ to each model PARSEC grid-point $\{T_{\text{eff}}, M_*, t\}$ via

$$\Delta^2 = \left(\frac{\tilde{T}_{\text{eff}} - T_{\text{eff}}}{\sigma_{\tilde{T}_{\text{eff}}}} \right)^2 + \left(\frac{\tilde{M}_* - M_*}{\sigma_{\tilde{M}_*}} \right)^2 + \left(\frac{\tilde{t} - t}{\sigma_{\tilde{t}}} \right)^2, \quad (8)$$

where the division by the uncertainties helps to assign equal importance to each dimension. The mass reported in Table 1 is the model mass that minimizes the distance. The reported uncertainties in the masses are based on propagating the statistical uncertainties in the radii, temperatures, and ages.

2.3.3. Binarity

The main types of binaries of interest in this work are those that are unresolved, because they can lead to misinterpretations of the data. For instance, unresolved binaries might produce multiple photometric signals and hinder our ability to correctly identify the star hosting the CPV signal. Unresolved binaries could also bias photometric magnitude and color measurements, which would affect our stellar parameter estimates. To attempt to identify binaries, we considered the following lines of information.

Radial velocity scatter—We examined diagrams of the Gaia DR3 “radial velocity error” as a function of stellar color for all 63 CPVs and candidate CPVs. Since this quantity represents the standard deviation of the non-published Gaia RV time series, outliers can suggest single-lined spectroscopic binarity. These plots showed two clusters of stars, at $\lesssim 10 \text{ km s}^{-1}$ and $20\text{--}25 \text{ km s}^{-1}$. We therefore adopted a threshold of 20 km s^{-1} to flag possible single-lined spectroscopic binaries, which selected three stars: TIC 405910546, TIC 224283342, and TIC 280945693.

RUWE—We examined plots of Gaia DR3 RUWE as a function of color.³ Elevated RUWEs imply excess astrometric noise relative to a single-source model. This can be caused by marginally resolved binaries, intrinsic photometric variability, or intrinsic astrometric motion. Based on this exercise, we adopted a threshold of $\text{RUWE}_{\text{DR3}} > 2$ to flag sources with excess astrometric noise. This threshold was met by 16/50 high-quality CPVs and by 0/13 of the ambiguous CPVs. The choice of the threshold RUWE is somewhat subjective, since the RUWE distribution has an extended tail (e.g. Penoyre et al. 2022). If we had instead required $\text{RUWE}_{\text{DR3}} > 1.4$, 21/50 high-quality CPVs and 2/13 of the ambiguous sample would have been flagged.

Gaia DR3 non-single stars—Gaia DR3 included a non_single_star column that flagged eclipsing, astrometric, and spectroscopic binaries. None of the stars in our CPV sample were identified as possible binaries in this column.

Multiple periodic TESS signals—During our visual analysis of the TESS light curves and PDM periodograms, we flagged sources with beating light curves, and with PDM periodograms that showed multiple periods. For such cases, we then subtracted the mean CPV signal over each sector, and repeated the phase-dispersion minimization analysis. The resulting secondary periods, P_{sec} , are listed in Table 1; we required these to be at least 5% different from the primary period. The majority of secondary signals showed morphologies corresponding to starspot modulation. This process yielded 22/50 high-quality CPVs with secondary periods; 3/13 of the ambiguous sample met the same criterion. Of the 16 good CPVs with $\text{RUWE}_{\text{DR3}} > 2$, 15 also showed secondary periods in the TESS light curves. Considering the weaker threshold of $\text{RUWE}_{\text{DR3}} > 1.4$, 18/21 such CPVs showed secondary TESS periods. The latter results strongly suggest that the secondary periods are associated with bound binary companions.

Table 1 summarizes each of the sources of binarity information into a single bitwise column. We describe detailed results concerning binarity in Section 3.4, and summarize those results Section 5.2.

3. RESULTS

3.1. CPV catalog

Table 1 lists the 66 objects identified by our search. The 50 stars in the “good” sample demonstrated what we deemed to be the key characteristics of the CPV phenomenon in at least one TESS sector. The classification of 13 CPV candidates was ambiguous, and the 3 remaining objects were notable false positives that we discuss below. The quality column in the table divides the three classes; additional data from TESS or other instruments could help resolve the classification of the ambiguous cases. Of the 63 CPVs and candidate CPVs, 32 were found using both the dip-counting and Fourier techniques, 23 were found using only the dip-counting technique, and 8 were found using only the Fourier technique. In the following, we will focus our discussion on the good sample, irrespective of discovery method. We will often refer to stars by their TIC identifiers; these can be referenced against the figures in most digital document readers using a “find” ($\text{Ctrl}+\text{F}$) utility.

Figure 4 is a mosaic of phased light curves for the 50 CPVs. The objects are sorted first in order of the number of TESS 2-minute cadence sectors in which they clearly demonstrated the CPV phenomenon, and secondarily by descending brightness. The top five objects by this metric are TIC 300651846 (12 sectors); TIC 402980664 (7 sectors); TIC 89463560 (5 sectors); TIC 363963079 (5 sectors); and TIC 294328887 (4 sectors). The brightest five CPVs span $9.3 < T < 11.1$; the faintest five span $14.5 < T < 15.0$. The fastest five have periods spanning $3.6 \text{ hr} < P < 6.2 \text{ hr}$, and the slowest five span $27 \text{ hr} < P < 38 \text{ hr}$.

The light curves show between two and eight local minima per cycle. Some stars show ordinary sinusoidal modulation during one portion of the phased light curve, and highly structured modulation in the remainder of the cycle

³ For an explanation of the renormalized unit weight error (RUWE), see the GAIA DPAC technical note http://www.rssd.esa.int/doc_fetch.php?id=3757412.

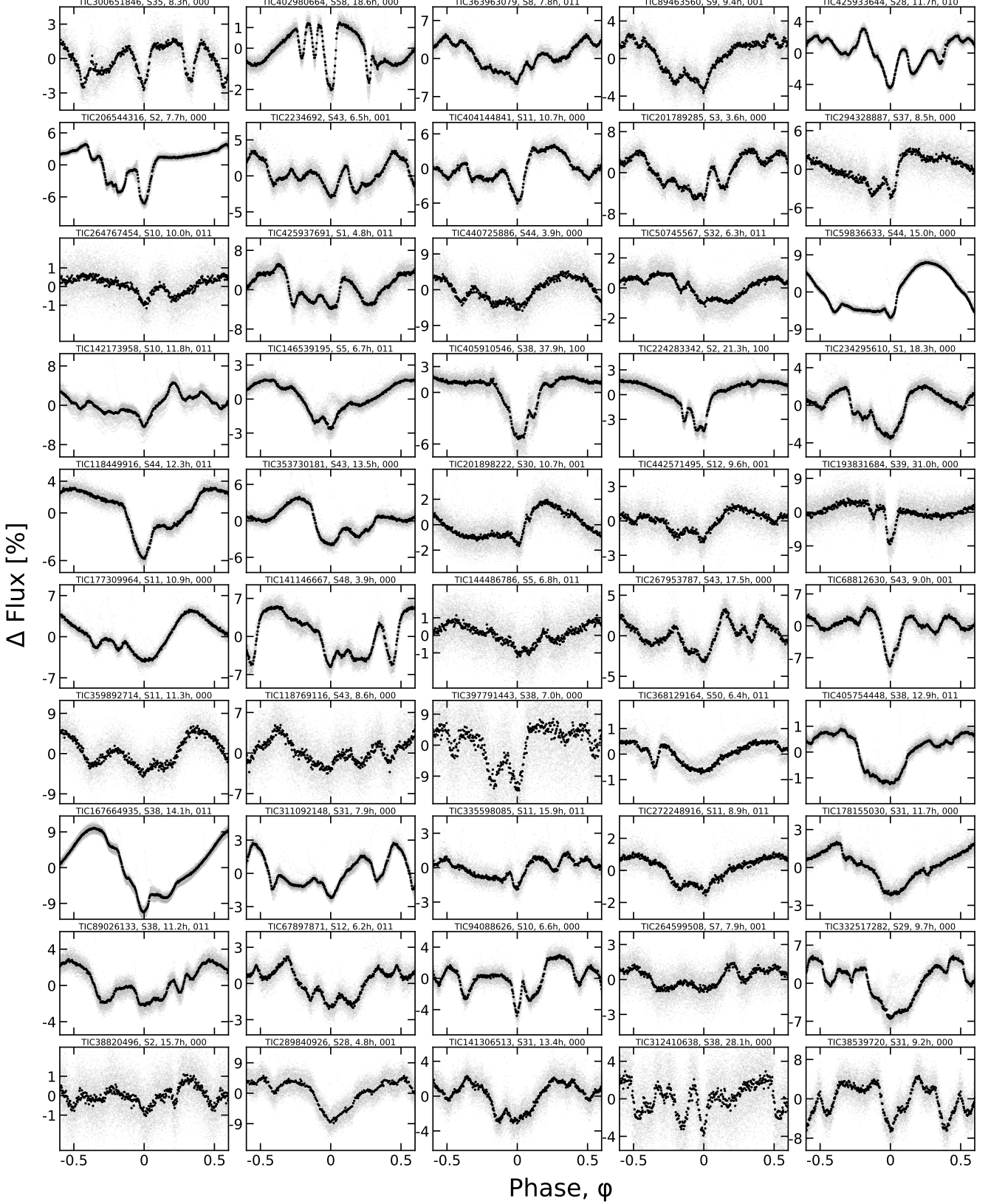


Figure 4. CPVs found in the TESS 2-minute data. Phased TESS light curves over one month are shown for 50 CPVs in the high quality sample. Gray are raw 2-minute data; black bins to 300 points per cycle. Objects are ordered such that sources with the most TESS data available are on top (see Section 3.1). Zero phase is chosen to correspond to minimum light. Each panel is labeled by the TIC identifier, the TESS sector number, the period in hours, and the three-bit binarity flag from Table 1, which denotes Gaia DR3 `radial_velocity_error` outliers (bit 1), Gaia DR3 `ruwe` outliers (bit 2), and stars with secondary TESS periods (bit 3).

(e.g. TIC 206544316, TIC 224283342, TIC 402980664). Others show structured modulation over the entire span of a cycle (e.g. TIC 2234692, TIC 425933644, TIC 142173958). Others show some mix between these two modes.

A small number of objects at first glance seem reminiscent of eclipsing binaries, such as TIC 193831684, TIC 59836633, or TIC 5714469. We believe these cases are unlikely to be eclipsing binaries due to the additional coherent peaks and troughs in the light curves, which are distinct from any binary phenomena of which we are aware.

3.2. Ages of CPVs

Of our 63 confirmed and candidate CPVs, 61 were associated with a nearby moving group or open cluster, primarily using BANYAN Σ as described in Section 2.3.⁴ The relevant groups are listed in Table 1; their ages span \approx 5–200 Myr. For comparison, BANYAN Σ assigned high-probability ($>95\%$) field membership to 59,361 out of the 65,760 target stars. Most stars in our target sample are old; the CPVs returned by our blind search are young.

The groups that contain the largest number of CPVs in our catalog are Sco-Cen, Tuc-Hor, and Columba. Six CPVs were also identified in the Argus association (Zuckerman 2019), which serves as an indirect line of evidence supporting the reality and youth of that group. The large contribution from Sco-Cen is not surprising since Sco-Cen contains the majority of pre-main-sequence stars in the solar neighborhood, and many of its stars were selected for TESS 2-minute cadence observations by guest investigators. Given the $\lesssim 10\%$ completeness of TESS beyond 100 pc (Figure 2), there may be many more CPVs in Sco-Cen that remain to be discovered.

There were two stars for which neither BANYAN Σ nor a literature search led to a confident association with any young group. Both stars display CPV signals over multiple TESS sectors. Both are photometrically elevated relative to the main sequence, an indication of youth. Both were also noted by Kerr et al. (2021) as being in the “diffuse” population of <50 Myr stars near the Sun.

Our search confirms that the CPV phenomenon persists for at least ≈ 150 Myr. Table 1 includes three ≈ 150 Myr CPVs in AB Dor (Bell et al. 2015), a ≈ 112 Myr old Pleiades CPV (Dahm 2015), and a similarly-aged Psc-Eri member (Ratzenböck et al. 2020). To our knowledge, TIC 332517282 in AB Dor ($t=149^{+51}_{-19}$ Myr; Bell et al. 2015) was the previous record-holder for the oldest-known CPV (Zhan et al. 2019; Günther et al. 2022); at least one unambiguous CPV (EPIC 211070495) and a few other candidates were also previously known in the Pleiades (Rebull et al. 2016).

The maximum age of CPVs might even exceed 200 Myr, based on the candidate membership of TIC 294328887 in the Carina Near moving group (Zuckerman et al. 2006). The esti-

mated age of this group, 200 ± 50 Myr, is based on the lithium sequence of its G-dwarfs (Zuckerman et al. 2006), which shows a coeval population of stars older than the Pleiades and younger than the 400 Myr Ursa Major moving group. However, the formal BANYAN Σ membership probability is somewhat low (only 6%), perhaps due to the missing radial velocity. This lack of information could be rectified by acquiring even a medium-resolution spectrum. An independent assessment of the group’s kinematics using Gaia data, and its rotation sequence using TESS, could also bear on the question of whether TIC 294328887 is a member.

3.3. Infrared excesses of CPVs

Most CPVs in our catalog did not show infrared excesses in the W1-W4 bands, which is typical for this class of object (Stauffer et al. 2017). Visually inspecting the SEDs of our 66 star sample and the WISE images available through IRSA, we labeled two objects as having reliable infrared excesses (both W3 and W4 fluxes are more than 3σ above the photospheric prediction): TIC 193136669 (TWA 34) and TIC 57830249 (TWA 33). However, neither is considered a “good” CPV for the reasons that follow.

Both of the stars with IR excesses are in the TW Hydrae association (≈ 10 Myr). They have periods of 38 hr and 44 hr, respectively. In our initial labeling, we labeled both as “ambiguous” CPVs because the dips in their Sector 36 light curves seemed to stochastically evolve over only one or a few cycles, which is atypical for CPVs; their periods were also long in comparison with most of the other CPVs. Inspection of additional sectors clarified that both sources are dippers, not CPVs (see the online plots in Figure 3). For TIC 57830249, the Sector 10 light curve shows completely different behavior from Sector 36, with variability amplitudes of $\pm 50\%$ and no obvious periodicity. TIC 57830249 also shows continuum emission at 1.3 mm (Rodriguez et al. 2015), which suggests that cold dust grains are present.

The dipper classification of TIC 193136669 is less obvious; the main indication that it is a dipper is that Sectors 62 and 63 show its dips appearing and disappearing within the span of one cycle. None of the CPVs in our sample exhibit this property. Independently, TIC 193136669 is known to have a cold disk of dust and molecular gas, based on 1.3 mm continuum emission and resolved $^{12}\text{CO}(2-1)$ emission (Rodriguez et al. 2015). It was labeled a dipper by Capistrant et al. (2022); we agree with their designation, and label it an “impostor” CPV in Table 1. Section 5.9 highlights plausible evolutionary connections between CPVs and dippers in light of these “misclassifications”.

3.4. Binarity of CPVs

3.4.1. Binary statistics

A significant fraction of the CPVs show indications of unresolved binarity. Excess noise above the Gaia single-source astrometric model is common (16/50 high-quality CPVs have $\text{RUWE}_{\text{DR}3} > 2$), as is the presence of multiple periods in the TESS light curves (22/50). Elevated astrometric noise almost always implies multiple detectable TESS

⁴ Two of the 61 memberships were made with low confidence and are flagged in Table 1. The assignment of TIC 397791443 to IC 2602 was based not on BANYAN Σ but instead on a literature search (e.g. Cantat-Gaudin & Anders 2020).

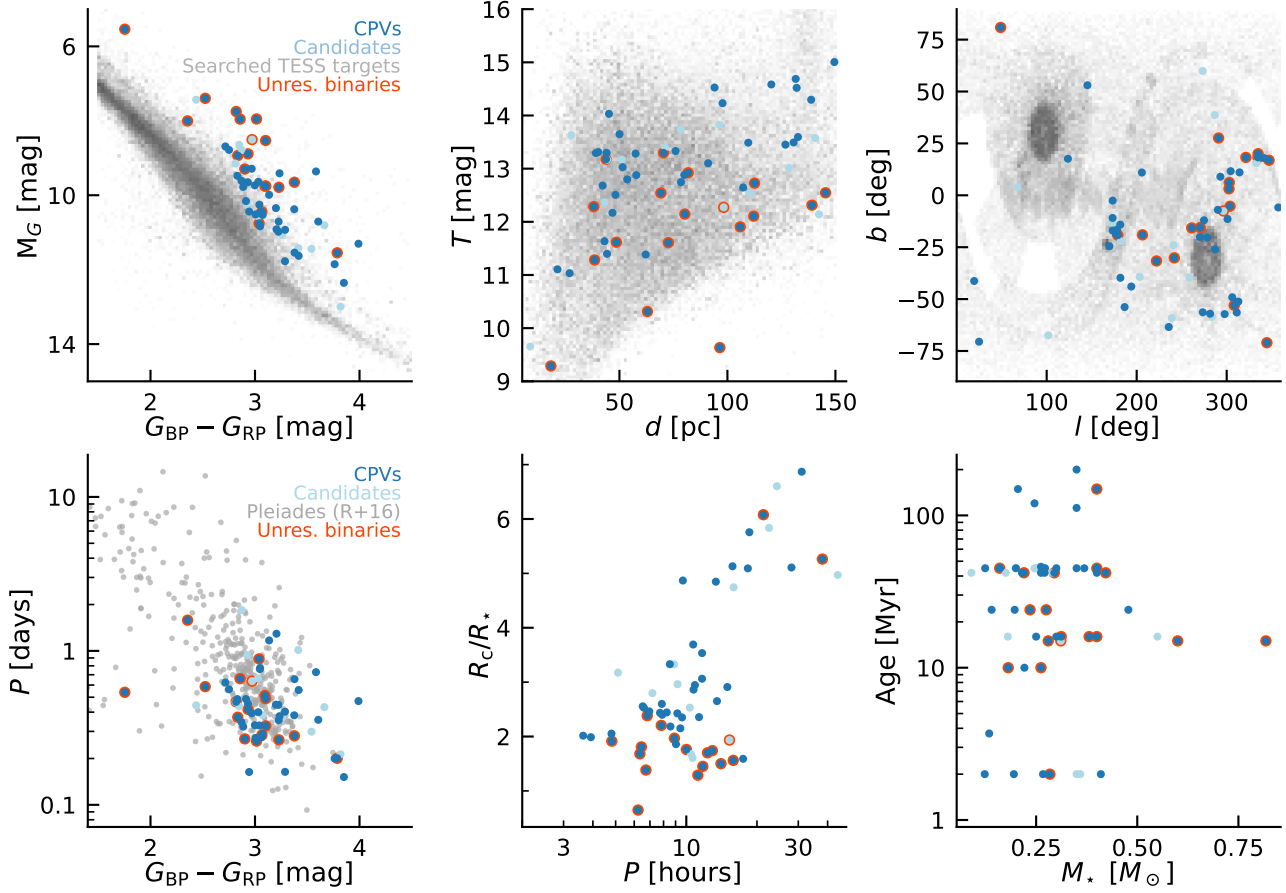


Figure 5. Properties of CPVs identified by our search. CPVs are mostly pre-main-sequence M dwarfs, younger than ≈ 150 Myr, with rotation periods faster than ≈ 1 day. The 50 bona fide CPVs in Table 1 are the dark blue dots; 13 ambiguous CPV candidates are light blue dots. Unresolved binaries (red rings) are objects for which the Gaia DR3 radial velocity scatter exceeded 20 km s^{-1} , or if $\text{Gaia RUWE}_{\text{DR3}} > 2$ and multiple photometric signals were present in the TESS light curve. The top panels show the 65,760 target stars with 2-minute cadence TESS data as the shaded gray background; darker regions correspond to a larger relative number of searched stars. The lower-left panel compares the rotation–color distribution of CPVs against the rotation periods of K and M dwarfs in the Pleiades from Rebull et al. (2016). The lower-middle panel plots the derived corotation radii $R_c = (GM/\Omega^2)^{1/3}$ in units of stellar radii against the measured CPV periods, in units of hours. Ages in the final panel are known from cluster membership.

periods (15/16 high-quality CPVs). The latter observation corroborates the claim that most sources with $\text{RUWE}_{\text{DR3}} > 2$ are binaries with projected apparent separations below $1''$, and projected physical separations $\lesssim 50$ AU. These observations are also in agreement with previous analyses of multi-periodic low-mass objects discovered by K2, which found that such systems are almost always binaries (Tokovinin & Briceño 2018; Stauffer et al. 2018a).

3.4.2. Do K dwarf CPVs exist?

To date, the only stars reported to show the CPV phenomenon are M dwarfs, with typical stellar masses $\lesssim 0.3 M_\odot$ (Stauffer et al. 2017; Günther et al. 2022). However the two most massive CPVs in our sample, TIC 405754448 and TIC 405910546, were assigned masses of $\approx 0.82 M_\odot$ and $\approx 0.60 M_\odot$ respectively. The next-highest mass in our sample

belongs to TIC 59836633 ($\approx 0.48 M_\odot$), with all remaining CPVs having masses $\lesssim 0.40 M_\odot$.

The locations of TIC 405754448 and TIC 405910546 in color–absolute magnitude diagrams, combined with their probable membership in Lower Centaurus Crux, support the conclusion that these stars have relatively high masses. However in detail, both objects are subject to ambiguities in interpretation. The TIC 405910546 light curve has a unique shape, suggestive of an eclipsing binary. Independently, TIC 405910546 was one of only three CPVs flagged with a Gaia DR3 radial velocity scatter exceeding 20 km s^{-1} . Combined, these factors suggest that TIC 405910546 could be a pre-main-sequence eclipsing binary; it should be studied further to clarify this classification.

For the other object, TIC 405754448, the evidence for binarity is stronger. The RUWE_{DR3} statistic is 6.8, and the raw light curves in Sectors 11, 37, and 38 show both the CPV

signal with period 12.9 hr and amplitude $\approx 1\%$ and an additional sinusoidal signal with a period ≈ 6.5 days and amplitude $\approx 0.3\%$, likely from a second star. If TIC 405754448 is a K+M binary, then the flux ratio between the primary and secondary would be expected to be $\approx 10:1$. Thus, if the K star were the source of the CPV signal, its intrinsic variability amplitude would be $\approx 1\%$, while if the M star were responsible its intrinsic variability amplitude would be $\approx 10\%$.

In short, these two objects suggest that the CPV phenomenon may extend up in mass to pre-main-sequence K dwarfs, but more data are needed to substantiate this claim.

3.4.3. An astrophysical CPV false positive: TIC 435903839

We originally classified TIC 435903839, with $\text{RUWE}_{\text{DR3}}=17.7$, as an “ambiguous” CPV with a 10.8 hr period, because this period minimized the dispersion in the phase-folded light curve. More careful inspection revealed an impostor: this source is a photometric blend of two ordinary rotating stars with $P_0=3.60$ hr, and $P_1=5.41$ hr, giving a beat period $(P_0^{-1} - P_1^{-1})^{-1}$ of 10.8 hr. This is a novel false positive scenario for CPVs: two rapid rotators near the 3:2 period commensurability. The beat between the two rotation signals produces the apparent CPV signal. Such false positives can be excluded through careful accounting of all peaks in a periodogram. For instance, TIC 435903839 shows a peak at 16.27 hr, which is not an integer multiple of the dispersion-minimizing 10.82 hr period.

3.4.4. Multiple CPVs in the same system: TIC 425937691 and TIC 142173958

TIC 142173958 and TIC 425937691 both show evidence for two separate CPV signals in their TESS light curves. For TIC 142173958, the signals have periods of 11.76 hr and 12.84 hr. For TIC 425937691, the two periods are 4.82 hr and 3.22 hr, near the 3:2 period commensurability. Given that both sources have two photometric signals and elevated RUWEs, each source is probably an unresolved binary consisting of two CPVs. To our knowledge, these are the third and fourth such systems known: EPIC 204060981 has two CPVs with periods of 9.59 hr and 9.12 hr (Stauffer et al. 2018b), and TIC 242407571 has two CPVs with periods of 11.33 hr and 13.63 hr, near the 6:5 period commensurability (Stauffer et al. 2021).

4. EVOLUTION OF CPV BEHAVIOR

4.1. Evolution over two year baseline

Figure 6 shows “before” and “after” views of 27 CPVs for which TESS 2-minute cadence observations were available at least two years apart. Such a baseline was available for 32 of the 50 confirmed CPVs in our catalog; for plotting purposes we show the brightest 27. We have defined $\phi = 0$ for each sector to be the time of minimum light observed in that sector, rather than using a consistent phase definition across multiple sectors. This is because for most of the sources we do not know the period at the precision necessary to be able to accurately propagate an ephemeris over two years. The

achievable period precision, σ_P , can be estimated as

$$\sigma_P = \frac{\sigma_\phi P}{N_{\text{baseline}}}, \quad (9)$$

for N_{baseline} the number of cycles in the observed baseline and σ_ϕ the phase precision with which any one feature (e.g. a dip, or the overall shape of the sinusoidal envelope) can be tracked. Assuming $\sigma_\phi \approx 0.02$ and a 20-day baseline over a single TESS sector yields $\sigma_P \approx 0.25^{+0.38}_{-0.14}$ minutes for the population shown in Figure 6; propagated forward 1,000 cycles yields a typical ephemeris uncertainty range of 2–11 hours. Measuring the period independently for each sector did not reveal evidence for significant ($>3\sigma$) changes in period, implying a period stability of $\lesssim 0.1\%$ over two years.

A few objects in Figure 6 show the CPV phenomenon in one sector, and only marginal signs or no sign of CPV behavior in the other sector. In our subjective assessment, cases for which at least one sector would be flagged as “ambiguous” include TIC 368129164 (Sector 23 might be labeled an EB), TIC 177309964 (Sector 38 would be simply a rotating star), TIC 404144841 (Sector 38 looks like a rotating star), TIC 201898222 (Sector 3 looks like a rotating star), TIC 144486786 (Sector 32 might be an RS CVn), and TIC 38820496 (Sector 28 might be an RS CVn). TIC 193831684, assessed on a single-sector basis, would probably be labeled an eclipsing binary—in fact, Justesen & Albrecht (2021) already gave this source such a label. However, based on the shape evolution between Sectors 13 and 39, it is a CPV.

Based on the fraction of sources that “turned off”, the observed shape evolution implies that CPVs have an on-off duty cycle of $\approx 75\%$. Correcting for the duty cycle might be important in population-level estimates of the intrinsic frequency of the CPV phenomenon (e.g. Günther et al. 2022).

4.2. Evolution over consecutive sectors, & LP 12-502

A few of our complex periodic variables were near the TESS continuous viewing zones (Figure 5, top right). Out of this already small sample, LP 12-502 (TIC 402980664; $d=21$ pc, $J=9.4$, $T=11.1$) stood out due to the quality and content of its data. We discuss another interesting source, TIC 300651846, in Appendix B. In this section, we describe the LP 12-502 observations and the possible implications.

4.2.1. LP 12-502 observations

Whenever LP 12-502 was located within a TESS sector, it was observed at 2-minute cadence. Figure 7 shows all the available data, from Sectors 18, 19, 25, 26, 53, 58, and 59. Vertical offsets were applied to separate the data from different spacecraft orbit numbers; there are always two orbits per sector. We binned the light curve to 15-minute intervals to facilitate visual inspection. Points more than 2.5σ above the median are drawn in gray, to prevent outliers from seizing attention. Data gaps are not connected by lines (a common source of confusion in light curve visualization). Figure 8 shows the same data after phase-folding each TESS

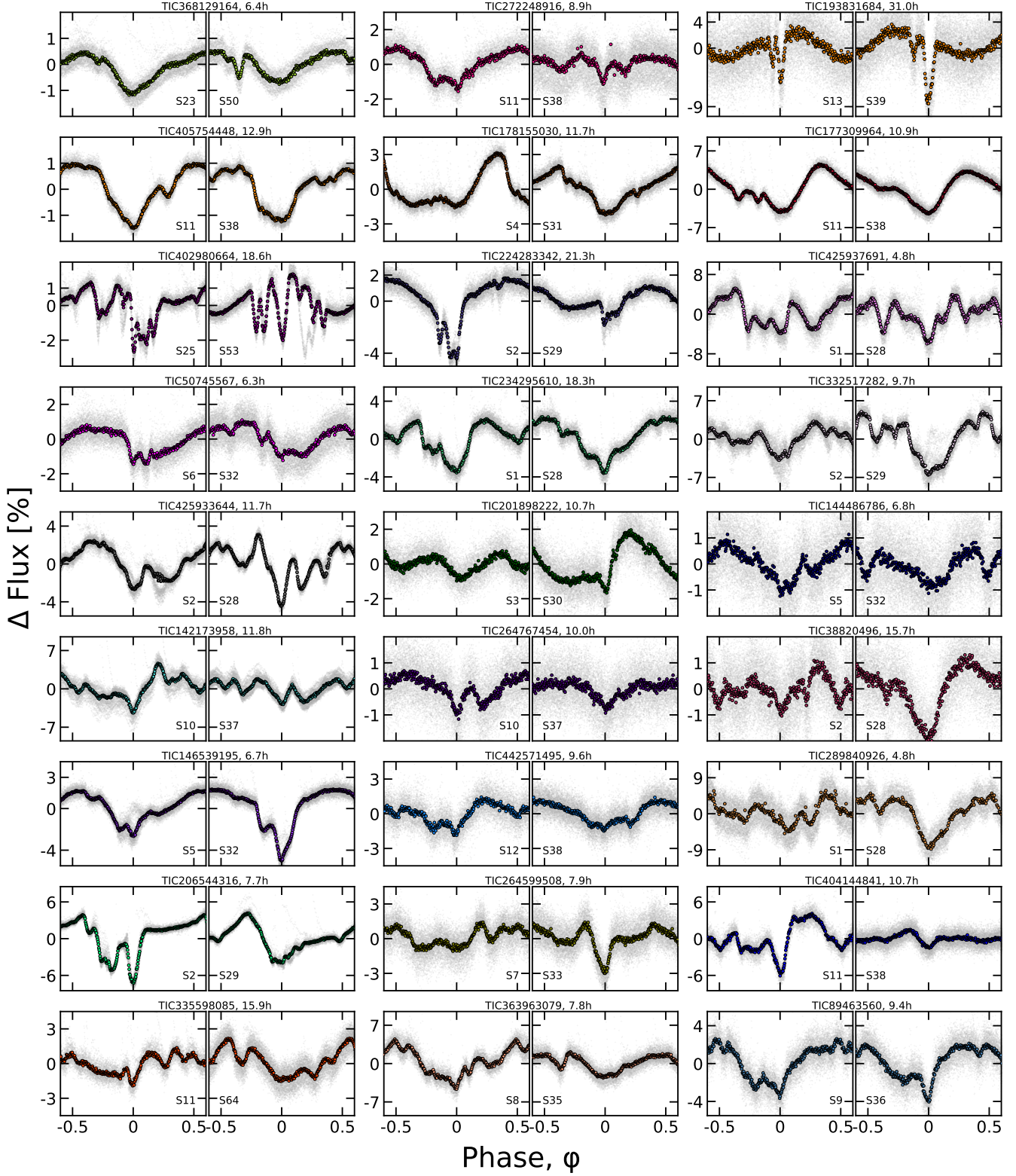


Figure 6. Evolution of CPV light curves over two years. Out of the 50 CPVs in Figure 4, 32 had 2-minute cadence TESS data available for a baseline of at least two years; the 27 brightest are shown here due to space constraints. Each panel shows one sector of TESS data, and is phased to its deepest minimum in flux. Each panel's title shows the TIC identifier and period in hours. Text insets show the TESS sector numbers, which generally span two years, or at least 1,000 cycles. The vertical scale is fixed across sectors to clarify shape changes. Gray circles are raw 2-minute data; colored circles bin to 300 points per cycle.

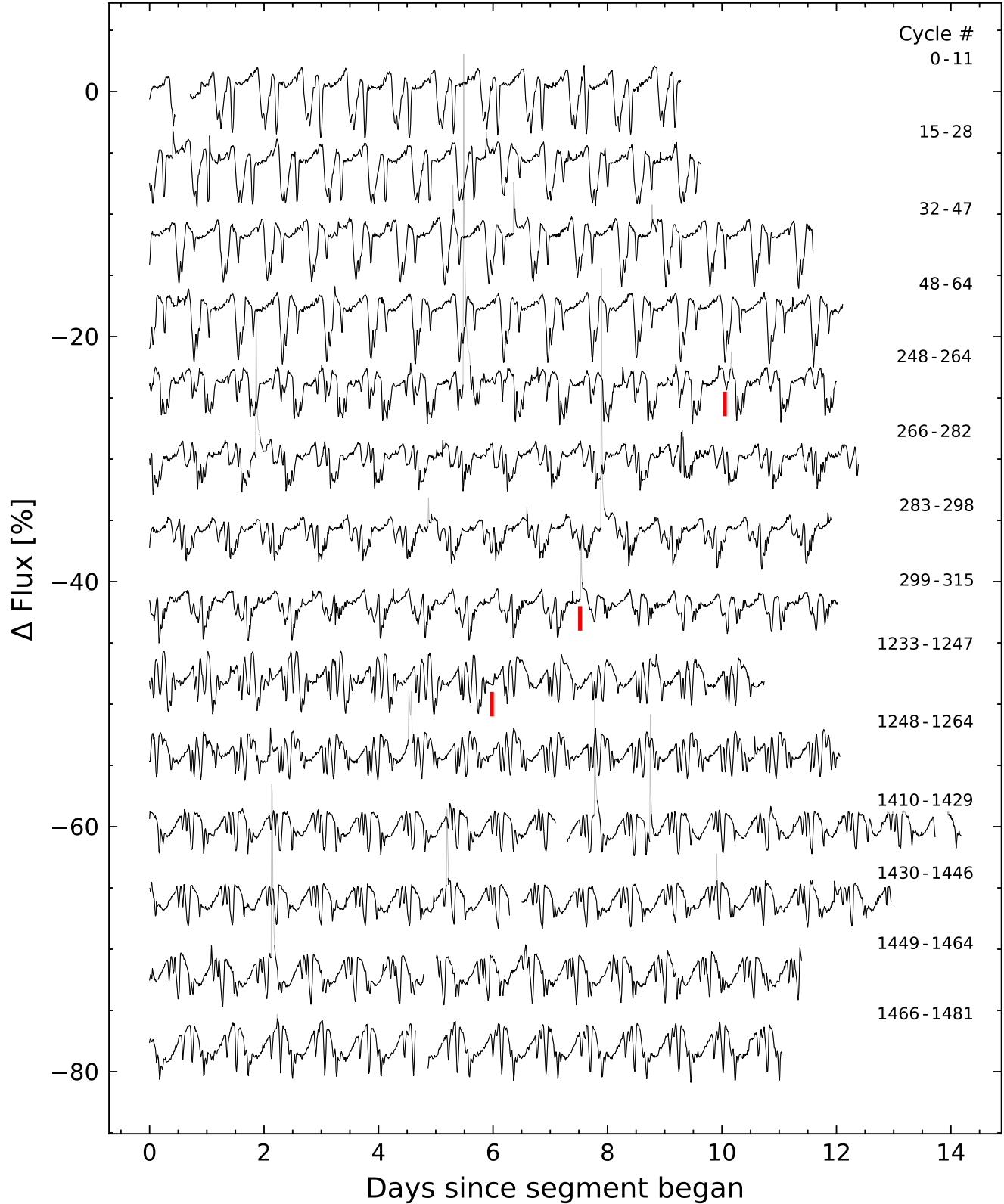


Figure 7. LP 12-502 (TIC 402980664) light curve, where each time segment represents one TESS orbit. Data were acquired in Sectors 18-19, 25-26, 53, and 57-58. Flares are drawn in gray. The light curve is binned to 15-minute intervals so that there are 96 points per day, and each point is connected by a line. Data gaps have nothing plotted. The red vertical lines highlight apparently instantaneous state changes in the shape of the dip pattern.

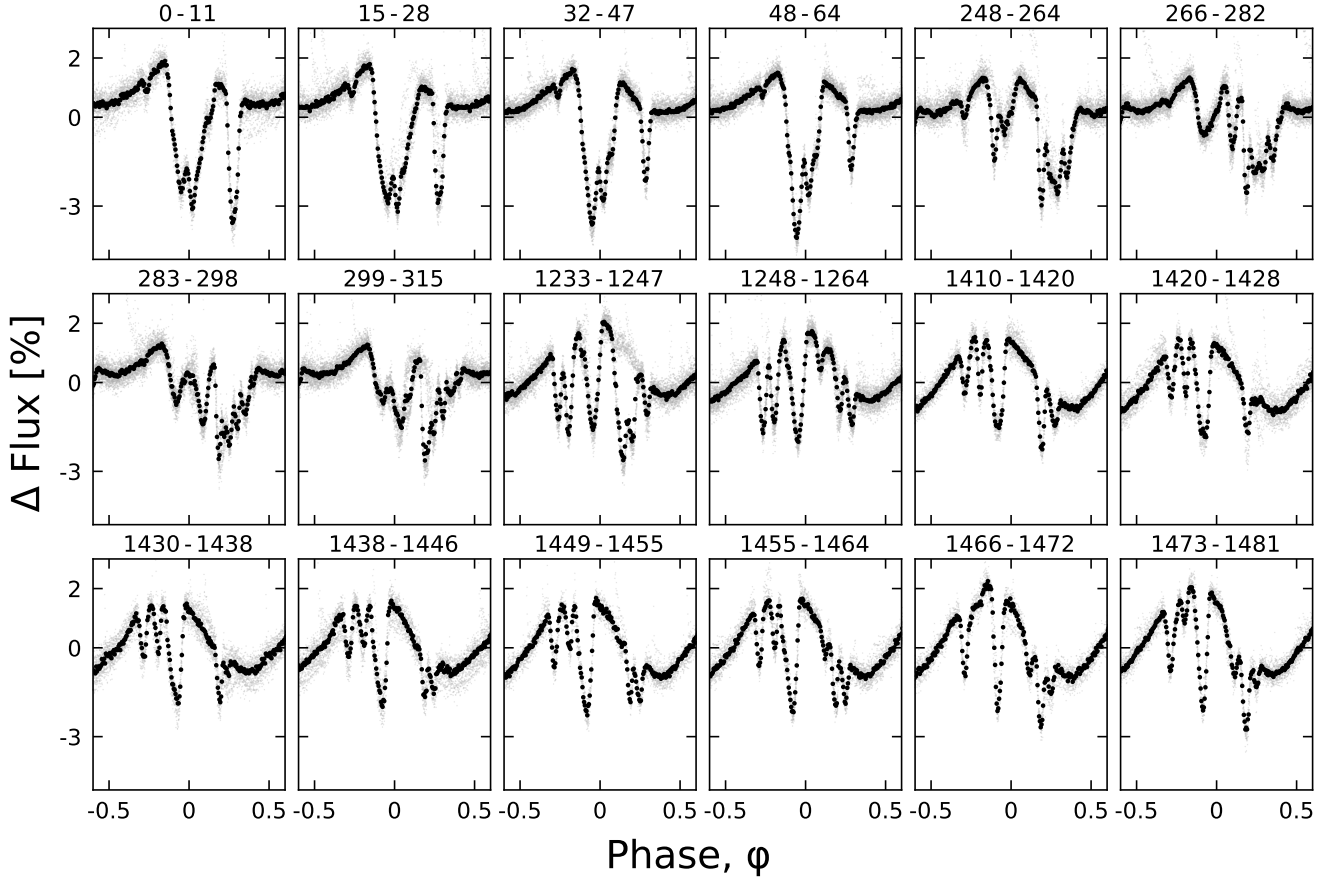


Figure 8. Evolution of LP 12-502 ($P=18.5611$ h) at fixed period and epoch over three years. Each panel shows one (averaged) TESS orbit; small text denotes relative cycle number. There are 200 binned black points per cycle. The TESS pointing law dictates the large time gaps between cycles 64–248, 315–1233, and 1264–1410; larger gaps tend to yield larger shape changes. The dips usually evolve over tens to hundreds of cycles. However cycles 1233–1264 show a dip that switched from a depth and duration of 3% and 3 hr to 0.3% and 1 hr over less than one cycle (cf. Figure 7).

spacecraft orbit, assuming $P=18.5611$ hr and a fixed reference epoch of BTJD=1791.5367. Finally, Figure 9 shows “river plots” of the same data, split into similar intervals: the Sector 18–19 data, 25–26 data, 53 data, and 58–59 data. The river plots are subject to one additional processing step: we fitted and subtracted a maximum-likelihood two-harmonic sinusoid independently from the Sector 18–19 data, 25–26 data, and 53, 58, and 59 data in order to accentuate changes in the dip timing and structure.

The average period, determined by measuring the PDM peak period over each sector independently, was $\langle P \rangle = 18.5560$ hr. The range between the maximum and minimum sector-specific periods was measured to be about one minute. However, a period shift of ± 1 minute leads to large phase drifts over the entire timespan of observations. One minute is $\approx 1/1000^{\text{th}}$ of a period, and we have observed 1500 cycles. By folding with a fine grid of trial periods, we found that the choice $P = 18.5611 \pm 0.0001$ hr causes more of the features in the LP 12-502 light curve to maintain constant phases over the entire dataset.

We now attempt to describe the complex morphology of the light curve and its evolution. For the first 64 cycles, the star shows four obvious local minima. We dub these dips $\{1, 2, 3, 4\}$ at phases $\{-0.28, -0.08, 0, 0.25\}$, respectively. Dips 2 and 3 are part of the same “global” minimum, which otherwise resembles a long eclipse. Over cycles 0–64, the depth of dips 1 and 3 remain roughly fixed. Dip 4 decreases in depth by about 2%, and dip 2 increases in depth by about the same amount (see Figure 8). A subtle fifth dip may also be present at phase +0.08, at the end of the global minimum that includes dips 2 and 3.

There is then a 6-month (184-cycle) gap to Cycles 248–315, which show two highly structured dip complexes, plus a small leading dip. The leading dip has the same phase (relative to minimum light) as in cycles 0–64, and therefore seems likely to be due to the same structure. Along a similar line of logic, it seems plausible that the first “dip complex” during cycles 248–264 represents an evolution and reduction in amplitude of dips 2 and 3 that were seen during cycles 0–64. During cycles 266–310, an additional local minimum devel-

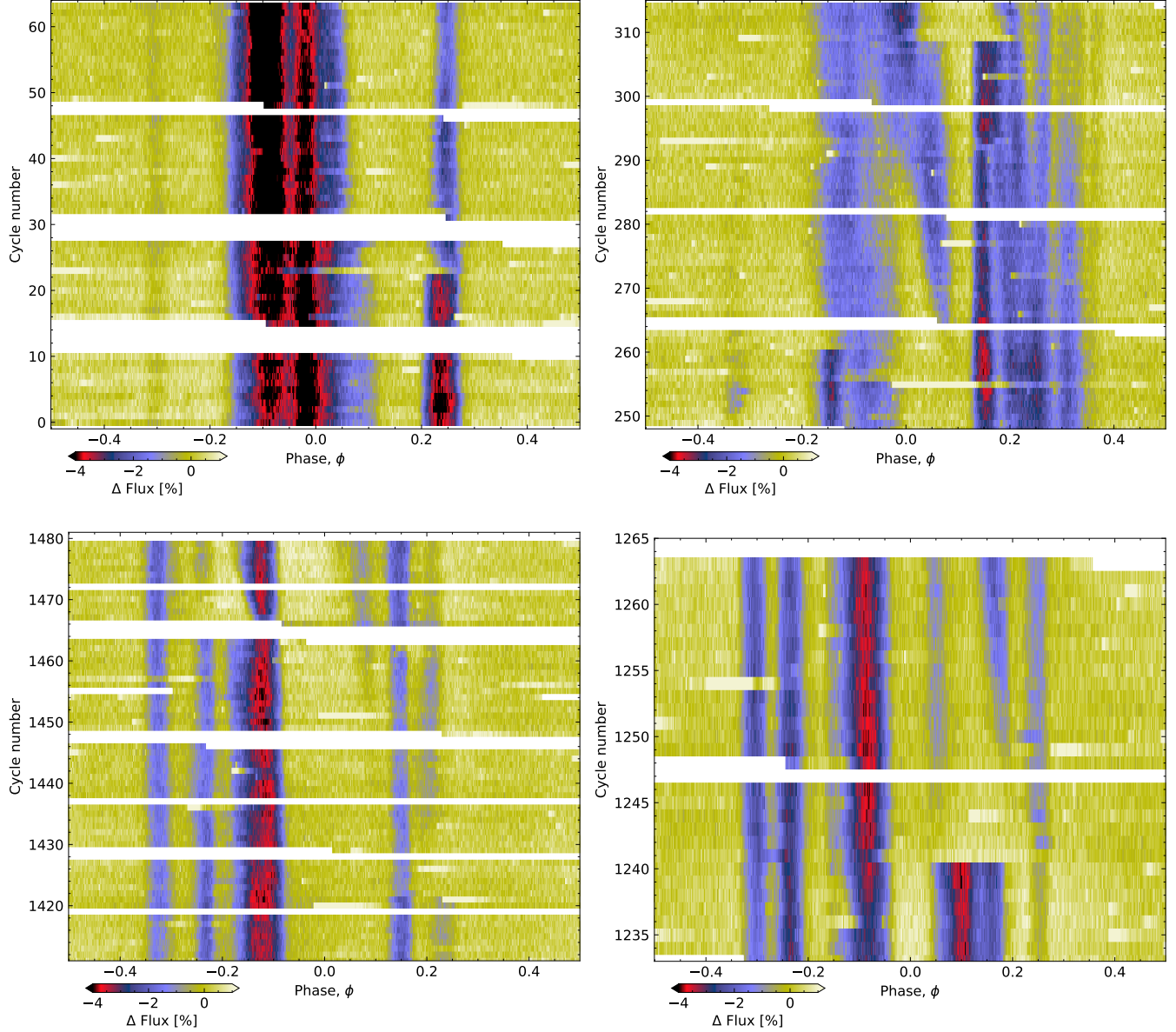


Figure 9. River plots of the LP 12-502 light curve, showing (clockwise from top-left) Sectors 18-19, 25-26, 53, and 58-59. A two-harmonic sinusoid has been subtracted to highlight the sharp dips. A fixed period and phase are adopted for all sectors; the dips across all observations are bounded by $\phi \in [-0.35, 0.35]$. In Sectors 25-26 (cycles 248-315), periods are visible at the fundamental period of 18.5611 hr, as well as at faster ($\phi \approx 0.07$) and slower ($\phi \approx 0.25-0.27$) relative periods based on the presence of blue dips with distinct slopes. Multiple simultaneous periods are also visible in Sector 53 (cycles 1234-1263) and Sectors 58-59 (cycles 1411-1479). White chunks denote missing data. The state changes noted with red markers in Figure 7 occur in cycles 261, 309, and 1241.

ops between the two complexes; this feature is best visualized on the river plots (Figure 9), where it is seen to have a shorter period than the other dips (as described below).

The second dip complex during cycles 248-315 shows the most substructure. During e.g. cycles 283-298, this single complex shows six local minima. The first and deepest dip is sharp: it shows a flux excursion of 3.5% over about 22 minutes ($0.02 P$), which is the steepest slope exhibited anywhere in the LP 12-502 dataset. After the sharp dip, there is a roughly exponential return to the baseline flux spanning

about a quarter of a period, punctuated by coherent local minima and maxima that the river plot (Figure 9) reveals to have slightly longer periods than the sharp dip. The sharp leading dip remains roughly constant in amplitude until a sudden “state change” at BTJD 2030.7 (cycle 309) that occurred at the same time as a flare, and left the trailing dips seemingly unaffected. This apparent state change, and two others, are marked with red lines in Figure 7.

The behavior during Sectors 53-58 (cycles 1233-1481) is comparatively tame; the light curve shows only four to six

dips per cycle. Some dips remain stable in depth and duration over this five-month interval. Other dips grow, like the one at $\phi = +0.06$ between cycles 1458 and 1481. Other dips, such as the one at $\phi = +0.12$ in cycles 1233-1264, disappear entirely. The most dramatic state change occurs during cycle 1241, when a large dip switches from a depth of 3% and a duration of 3 hours to a depth of 0.3% and a duration of 1 hour.

4.2.2. Lessons from LP 12-502

STATE-CHANGES REVEAL DIP INDEPENDENCE—The state-changes seen in cycles 261, 309, and 1241 confirm that dips can disappear in less than one cycle. While such behavior was also noted by Stauffer et al. (2017), the data presented here show further that the dips can be *independent* and *additive*. For example, throughout cycles 1233-1264, there are three sharp dips between phases of 0 and 0.3 with different amplitudes but similar slopes. During the transition, the leading dip nearly disappeared while the other two dips hardly changed; compare the centermost two panels of Figure 8. Evidently, the material or process responsible for one dip can vary independently of the materials or processes responsible for other dips. The state changes during cycles 261 and 309 support the same conclusion, while also hinting that the *leading* dip of a complex is most prone to disappearing, leaving the trailing dips unchanged in its wake.

SLOW GROWTH; RAPID DEATH—LP 12-502 shows at least three instances in which dips switch off over less than one cycle; we did not see any such instances of dips switching on. Dip growth seems to happen more slowly. For instance, the dip at phase 0-0.1 between cycles 258-290 begins to become detectable during cycle 258, and grows in depth by about 2% over the next eight cycles. The evolution of this particular dip is most clear in the river plots. The evolution of the dip group at phases 0.1-0.3 during cycles 1410-1481 is another example of this slow mode of dip growth.

DIP DURATIONS—The shortest dip duration for any of the individual LP 12-502 dips seems to be $\approx 0.06 P \approx 1.08$ hr. This is very similar to the characteristic timescale of a transiting small body at the corotation radius,

$$T_{\text{dur}} \equiv R_* P_{\text{rot}} / (\pi a) = 1.02 \pm 0.10 \text{ hr}, \quad (10)$$

where we have inserted the stellar radius and mass derived in Section 2.3. Thus, the shortest-duration dips are likely produced by transits of bodies or distributions of material that are smaller than the star. The corotation radius corresponds to $a/R_* \approx 5.8$, i.e., the transit of a body at the corotation radius has a duration about six times shorter than a feature on the stellar photosphere that is carried across the visible hemisphere by rotation. On the other hand, some dip durations are sufficiently long that an explanation involving transits would require structures that are larger than the star along the direction of orbital motion.

DIP PERIODS—Most of the LP 12-502 dips repeat with a period of $P = 18.5611 \pm 0.0001$ hr. However the river plots (Figure 9) reveal that a few dips have detectably distinct periods. For instance, in sectors 25-26, the dip that develops

around cycle 262 has a period shorter than the mean period by $\approx 0.1\%$, and some of the trailing local minima in the main dip complex have periods slower than the mean period by $\approx 0.04\%$. In addition to the fundamental period, we were able to identify at least four distinct periods shown by specific dips over the full Sectors 18-59 dataset: 18.5683, 18.5672, 18.5473, and 18.5145 hr, with a measurement uncertainty of ≈ 0.0002 hr. Possibly, the different periods belong to clumps of dust or prominences of gas at slightly different orbital distances surrounding the corotation radius.

5. DISCUSSION

5.1. Typical and extreme CPVs

Referring back to Figure 5, typical CPV masses span $0.1 - 0.4 M_\odot$, typical ages span 2-150 Myr, and relative to the Pleiades, the CPVs are among the more rapidly rotating half of M dwarfs. The CPV mass and age range includes both fully convective stars and stars with a combination of radiative cores and convective envelopes; the dividing line for these ages is at around $M_* = 0.25 M_\odot$ (Baraffe & Chabrier 2018). We found no obvious differences in light curve morphology for CPVs above and below this fully-convective pre-main-sequence boundary.

The closest CPV in our catalog is DG CVn (TIC 368129164), a member of AB Dor at $d=18$ pc. The three brightest CPVs are DG CVn ($T=9.3$), TIC 405754448 ($T=9.6$), and TIC 167664935 ($T=10.3$). The shortest period, 3.64 hr, belongs to TIC 201789285. The longest period, 37.9 hr, belongs to TIC 405910546. Based on the Gaia DR3 RV scatter, the latter source may turn out to be an eclipsing binary; if so, the longest-period CPV in our catalog would be TIC 193831684 (31.0 hr). By definition, we required the periods to be below 48 hr.

The lowest mass ($\approx 0.12 M_\odot$) belongs to TIC 267953787. The catalog contains a few other stars with similar mass. We cannot rule out the possibility that CPVs exist with even lower masses, given the small number of such low-mass stars in our target sample. Perhaps even brown dwarfs can be CPVs, although it might be difficult to distinguish the type of variability we associate with CPVs from the usual variability of brown dwarfs caused by clouds and latitudinal bands (e.g. Apai et al. 2021; Vos et al. 2022).

5.2. Is binarity important for CPVs?

For CPVs, binarity seems to provide either nuisances or curiosities. The nuisances include astrophysical false positives with two beating rapidly rotating stars, as well as uncertainty about which star produces the CPV signal in binary systems. Our two candidate K dwarf CPVs suffer from this latter concern (see Section 3.4).

Curiosities include the four binary systems that are now known to each host two separate CPVs. CPVs are sufficiently rare that such systems may have physical import. Recent work has shown that the orbits of binaries closer than $\lesssim 700$ AU tend to be aligned with their planetary systems (e.g. Christian et al. 2022). If we assume that observing CPV variability requires high line-of-sight inclinations, and that

the inclinations in binaries are correlated, then we would expect the detection of one CPV in a binary system to raise the probability that the other star is a CPV. The limitations of the current catalog prevent further exploration of this issue, but it might be interesting for future study.

A separate possible relation between binarity and CPVs is that the presence of a binary companion could cause early disk dispersal, freeing the star to contract. The CPV phenomenon seems to require rapid rotation; thus if binary systems tend to produce more rapidly rotating stars, we would expect a sample of CPVs to have a larger binary fraction than the field. However, we see minimal evidence for such an effect (Section 3.4). The multiplicity rate of M dwarfs near the Sun is $26.8 \pm 1.4\%$ (Winters et al. 2019). The $\approx 32\%$ multiplicity fraction in our CPV sample (from RUWE_{DR3}; see Section 3.4) seems approximately consistent with this field fraction.

5.3. Transience of CPV dips

While CPV periods appear to remain fixed over thousands of cycles, the light curve shapes evolve over typical timescales of 10 to 1,000 cycles (e.g. Figures 6 and 9). Although we refer to them as “periodic”, the CPVs are therefore actually quasiperiodic, with coherence timescales of ≈ 100 cycles. This marks a qualitative departure from the “persistent” vs. “transient” flux dip distinction previously described by Stauffer et al. (2017), which was based on $\lesssim 100$ cycle K2 baselines. The observation that CPVs have a population-averaged on-off duty cycle of $\approx 75\%$ (Figure 6) is also new. Appendix B for instance shows $\approx 1,000$ cycles of a source, TIC 300651846, with between zero and five sharp local minima per cycle. During the “zero” epochs (cycles ≈ 503 -542), the source would likely be labeled an ordinary rotating star.

5.4. Special phases of CPV dips

An independent peculiarity of CPV evolution is that the dips do not explore all phase angles with equal weight. LP 12-502, and other CPVs, exhibit preferred phases lasting for at least two years. For LP 12-502, all of the dips happen over phases corresponding to only two thirds of the period (Figures 8 and 9). The remaining third seems to be “out of limits” for dips over the timespan of observations. This could be evidence that the stellar magnetic field is not azimuthally symmetric. Alternatively, the source of the material (e.g. a planetesimal swarm) might be distributed over an arc rather than occurring randomly around the entire orbit.

5.5. Dip asymmetries?

The asymmetry of a dip around the time of minimum light might be caused by the variation in optical depth of the occulting material as a function of orbital phase angle. Sharp leading edges with trailing exponential egresses, for instance, have been previously seen for transiting exocomets and integrating rocky bodies (e.g. Rappaport et al. 2012; Brogi et al. 2012; Vanderburg et al. 2015; Zieba et al. 2019).

Examining Figure 4, it is clear that CPV dips can be asymmetric but it is not obvious whether there is a preference for

sharper ingresses or sharper egresses. In some cases (e.g. TIC 425933644), the flux variations do not resemble isolated dips, making the meaning of “ingress” and “egress” unclear. In other cases, such as Sector 36 of TIC 89463560, there is a sharp drop with an exponential return to the baseline flux, resembling the signatures of exocomets (e.g. Rappaport et al. 2018; Zieba et al. 2019), and the outflowing exospheres of some transiting planets (e.g. McCann et al. 2019; MacLeod & Oklopčić 2022).

5.6. What causes the CPV phenomenon: dust vs. gas

Both the dust clump and the gas prominence scenarios (Figure 1 and Section 1) invoke clumps of material at the corotation radius; one property that distinguishes the two ideas is the composition of the material.

5.6.1. What is a prominence?

The prominence idea is based on a loose analogy with quiescent prominences/filaments in the solar corona that last as long as a few weeks (see Vial & Engvold 2015). In the context of the Sun, a prominence is a clump of cold, partially ionized hydrogen viewed in emission against the dark backdrop of space. A filament is the same clump of plasma, but viewed in absorption against the solar disk. In an extrasolar context, spectroscopic detections of transient Balmer- and resonance-line absorption seen for stars such as AB Dor and Speedy Mic (e.g. Collier Cameron & Robinson 1989; Jeffries 1993; Dunstone et al. 2006; Leitzinger et al. 2016) have been interpreted as prominences that scatter a star’s chromospheric emission (see Collier Cameron & Robinson 1989). The short-term mechanical stability of such gas configurations is theoretically plausible for rapid rotators (Ferreira 2000; Waugh & Jardine 2022). To our best knowledge, this class of spectroscopic observation also has no viable alternative explanations.

We performed a simple visual examination of the TESS light curves for five prominence-hosting systems studied by Jardine & Collier Cameron (2019)—AB Dor, Speedy Mic, LQ Lup, HK Aqr, and V374 Peg—and detected no CPV behavior. While individual prominences may only last one to tens of rotation cycles, the prominence system itself is thought to always be “on”, due to the repeatable detectability of spectroscopic transients (e.g. Collier Cameron et al. 1990, and references therein). Assuming that spectroscopically observable prominence systems indeed do not turn off, this would imply that they are not always accompanied by photometric CPV-like dips: a link between the spectroscopic prominences that may exist around rapidly rotating low-mass stars and the CPV phenomenon has yet to be made.

5.6.2. What is the microphysical source of opacity?

CPVs show broadband flux variations that can be 1-2× deeper in the blue than in the red (Onitsuka et al. 2017; Bouma et al. 2020; Günther et al. 2022; Koen 2023). Dust can naturally explain this chromaticity, since it has a larger absorption cross-section in the blue than the red (e.g. Cardelli et al. 1989). Gas might also explain the observed chromaticities (Gray 1992). While bound-bound absorption can be

excluded, since it provides opacity only at narrow resonant lines, the hydrogen opacity due to bound-free absorption is “jagged” (see Gray 1992, Figure 8.5 and Eq. 8.8), such that at temperatures of $\approx 3,000$ K to $\approx 10,000$ K the opacity can be larger at blue wavelengths than at red wavelengths. Bound-free absorption of H $^{-}$ is often important at such temperatures, but this opacity source is stronger in the red than the blue, the opposite of what is required to produce deeper dips in the blue than in the red. Likewise, Thomson scattering is too gray to be the dominant opacity source. From hydrogen alone, bound-free absorption therefore seems like the most plausible opacity source. However it remains to be demonstrated whether a sufficient population of excited states could be maintained, particularly given the short (\approx microsecond) radiative decay timescales.

An instructive point of comparison is the rapidly rotating magnetic B star, σ Ori E, which shows dips that are deeper in the blue than in the red (Hesser et al. 1977). Photometric and spectroscopic observations of this star have been understood in terms of a warped torus of corotating circumstellar material (Landstreet & Borra 1978; Nakajima 1985; Townsend et al. 2005). The circumstellar material is unlikely to be dust, which would sublimate quickly at the distance of the torus from the star.⁵ The opacity source for σ Ori E and its analogs is instead thought to be bound-free absorption by neutral hydrogen (Nakajima 1985), although to our best knowledge direct evidence for this conclusion has yet to be acquired. Separate and smaller-amplitude continuum flux brightenings in σ Ori E may also come from electrons scattering photospheric light toward the observer when the clouds are not transiting (Berry et al. 2022).

Given these complexities, it seems important for a future theoretical study to be conducted to determine to what degree the observed chromaticities in CPVs match, or do not match, expectations from radiative transfer. This issue has a key ability to resolve the question of whether the CPVs are explained by dust or by gas, which has bearing on whether the material producing the dips is coming from the star, or whether it is a byproduct of the protoplanetary disk.

5.6.3. The lifetime constraint

The observed lifetime of the CPV phenomenon could provide another way to discern between the gas and dust clump scenarios. Based on the available statistics from e.g. Rebull et al. (2022) and references therein, it seems plausible that CPV occurrence decreases with stellar age from $\approx 3\%$ at 10 Myr (Sco-Cen), to $\approx 1\%$ at 100 Myr (Pleiades), down to 0% by the ≈ 700 Myr age of Praesepe. This is odd in the context of the prominence scenario, because pre-main-sequence M dwarfs spin up over the first 100 Myr; prominences might therefore be expected to be *more* common at 100 Myr than at

10 Myr, under the assumption that the production of prominences depends only on the stellar rotation rate. The dust clump scenario would hold a natural explanation: the lower occurrence of CPVs around older stars would simply reflect a finite supply of dust. One possible complication however is that the magnetic field topology of rapidly rotating M dwarfs may depend on factors other than the rotation rate (e.g. the age), which might alter the production of prominences.

5.7. Planets or planetesimals near corotation?

Close-in planets are common around M dwarfs; studies from Kepler have shown that early M dwarfs have ≈ 0.1 planets per star with sizes between $1\text{--}4 R_{\oplus}$ and orbital periods within 3 days (Dressing & Charbonneau 2015). The frequency of planets per star increases to ≈ 0.7 when considering periods as long as 10 days. Extrapolating to all small ($0.1\text{--}4 R_{\oplus}$) planets within 10 days, it is reasonable to expect nearly all M dwarfs to have at least one planet.

In the context of disk-driven planet migration, the stopping location for the innermost planet is set by the protoplanetary disk’s truncation radius (e.g. Izidoro & Raymond 2018, and references therein). The truncation radius is often calculated by equating the magnetic pressure from the stellar magnetosphere with the ram pressure of the inflowing gas. As it happens, the truncation radius is close to the corotation radius for low accretion rates (e.g. Romanova & Owocki 2015; Li et al. 2022). These considerations invite us to imagine one or more planets migrating inward due to gas drag, and arriving at $\approx 5\text{--}10$ stellar radii before the disk is depleted.

With this picture in mind, it is tempting to attribute features of the CPV light curves to transits of material ejected by planets or planetesimals. Young rocky bodies are expected to be hot, and they might expel either gas or dust. The Jupiter-Io system (e.g. Saur et al. 2004) is analogous, in that a small rocky body feeds the construction of a plasma torus. We emphasize that although this type of configuration seems a priori plausible, no direct evidence currently supports it.

The main logical function of the planetesimals would be to serve as a source for the occulting gas or dust; they would not necessarily need to explain the observed phases of the observed dips. The azimuthal angle of the eventual entrainment could be entirely dictated by the stellar magnetic field. In this scenario, the obscuring material would inspiral from one or more rocky bodies well beyond the corotation radius. The planetesimals themselves would not necessarily need to transit. However if they did, they would need to be $\lesssim 1 R_{\oplus}$ based on their non-detections in the TESS data. Possibly analogous systems include K2-22 (Sanchis-Ojeda et al. 2015) and KOI-2700 (Rappaport et al. 2014), though the obscuring material in the CPVs would need to be observed much further from the emitting planet than for those two examples.

A more restrictive variant of the planetesimal scenario would be to posit that the obscuring material remains close to the launching body, similar to comets, or to the aforementioned K2-22 and KOI-2700 systems. If so, then the planetesimals would need to be at the corotation radius. One prediction would therefore be that certain orbital phases would

⁵ Zhan et al. (2019) explored the sublimation timescales for a canonical CPV with $M_*=0.2 M_{\odot}$, $R_*=0.3 R_{\odot}$, and $T_{\text{eff}}=3200$ K. They found that non-shielded, generic silicate dust mixture (Draine 1985) with a single size of $0.1 \mu\text{m}$ reached the ≈ 1500 K sublimation temperature at $\approx 3 R_*$. This suggests that dust sublimation could be an important effect even for CPVs.

produce recurrent dips when observed over sufficiently long baselines, because the launching planetesimal would be massive enough to remain in orbit, while stochastically ejecting material. For most CPVs (Figure 6), the data seem to be in tension with this expectation because the relative spacing between dips is almost never conserved. With that said, certain sources do seem to exhibit “special phases”, including LP 12-502 (TIC 402980664), DG CVn (TIC 368129164), TIC 193831684, and TIC 146539195. One possible explanation for this might be if obscuring material is remaining close to its launching body, or bodies. An alternative explanation could be that the stellar magnetic field configurations responsible for confining said material are stable over the existing two-year baseline.

5.8. Mass flux estimate

Assuming for the moment that the obscuring material is dust, we can estimate the mass of a transiting clump. First, we convert the transit depth into an effective cloud radius, R_{cloud} . For most CPVs in Figure 4, this yields $\approx 2\text{-}20 R_{\oplus}$. A minimum constraint on the number density of dust particles is obtained by requiring the cloud to be optically thick. For cases like LP 12-502, this is reasonable because the transit duration of the shortest dips implies $R_{\text{cloud}} \ll R_{\star}$. Carrying out the relevant calculation assuming the dust grains are $1 \mu\text{m}$ in size, Sanderson et al. (2023) reported minimum cloud masses of order 10^{12} kg (their Eq. 23), which scale linearly with both the optical depth and dust grain radius. This is comparable to a small asteroid; the asteroid belt itself has a mass of order $\approx 10^{21} \text{ kg}$ (Park et al. 2019). A similar calculation that assumed occulting clumps of hydrogen, rather than dust, derived gas prominence masses of at least 10^{14} kg (Collier Cameron et al. 1990), about $100\times$ larger than the lower limit on the dust mass.

If the disappearance of a dip represents the permanent loss of the obscuring material – for example, if it is the result of a dust clump being accreted or ejected – then we can also estimate the rate at which mass is flowing through the structures that lead to dips. For instance, LP 12-502 showed three “state-switch” events over the six months of available TESS observations, during cycles 261, 309, and 1241 (Figure 9). The other source for which we performed a comparable analysis, TIC 300651846 (Appendix B), showed two state-switches over 11 months. In all such cases, at least one dip turned off. For purposes of estimation, we will take LP 12-502 as our prototype. Assuming the occulting material is dust, the corresponding $\dot{M} \equiv M \cdot dN/dt$ time-averaged over six months is $\approx 1 \times 10^{-12} M_{\oplus} \text{ yr}^{-1}$. Considered cumulatively over the $\approx 10^8$ years for which the CPV phenomenon is observed, this yields a cumulative moved dust mass of $10^{-4} M_{\oplus}$, of order the Solar System’s asteroid belt. If the occulting material is gas, the lower mass bounds would be of order 100 times larger. For cases in which we observe the growth of dips, such as the Sector 29 data for TIC 224283342, or Sector 5 of TIC 294328885, the dip depths typically increase by of order a few percent over ten to twenty days. This growth

rate yields a mass flux one order of magnitude larger than the earlier estimate.

5.9. From dippers to debris disks

About one in three young stars with infrared-detected inner dusty disks show quasiperiodic or stochastic dimming over timescales of roughly one day (e.g. Alencar et al. 2010; Cody & Hillenbrand 2010). The dimming amplitudes can reach a few tenths of the stellar brightness, and dips with identical depths and phases rarely recur. These “dipper” stars are probably explained by occulting circumstellar dust in the inner disk (e.g. Cody et al. 2014; Ansdel et al. 2016; Robinson et al. 2021; Capistran et al. 2022). While the phenomenon can persist beyond $\approx 10 \text{ Myr}$ (Gaidos et al. 2019, 2022), in all such cases it seems to be associated with the presence of infrared excesses. Phenomenologically, dippers are different from CPVs in that their dips are usually deeper, less periodic, and more variable in depth over timescales of only one or a few cycles. Dipper stars also tend to be younger, since they tend to be classical T Tauri stars with infrared excesses.

In identifying the two candidate CPVs with outlying SEDs (TICs 193136669 and TIC 57830249; Section 3.3), we were prompted to reconsider our light curve-based labeling, and ultimately concluded that these sources are dippers. This episode suggests that there could be overlap between CPVs and dippers. Taking TIC 57830249 as one example, the Sector 36 TESS data are suggestive of a CPV, with relatively periodic, sharp dips with depths of a few percent. The Sector 10 data are completely different, varying in apparent flux by a factor of two, with no discernible periodicity at all. Perhaps this source becomes a “dipper” when an inflow of dust reaches the inner disk wall, and is otherwise a “CPV” when the inner disk is starved of dust.

Although TIC 57830249 is an intriguing outlier, the general picture is that stars without infrared excesses have more stable optical light curves than those with infrared excesses. While some dippers may evolve into CPVs after the disk is mostly gone, this would be generically expected based on population statistics: young objects become old. There may be no other causal connection between the two evolutionary stages. With that said, a common mystery between the CPVs and dippers is how exactly the narrowness of their flux dimmings is produced. A similar mechanism may operate for both types of object, tied perhaps to a shared magnetic topology, or perhaps to a preference for dust to inspiral to the star in clumped structures.

5.10. Strengthening the magnetic B star connection

Stauffer et al. (2017) previously noted a possible connection between the CPVs and rapidly rotating magnetic B stars such as σ Ori E, which can have circumstellar gas clouds trapped in corotation (Townsend et al. 2005). The σ Ori class is distinct from Be-star decretion disks, which are found to systematically not host detectable magnetic fields (Rivinius et al. 2013; Wade et al. 2016).

An argument against the connection between CPVs and the σ Ori E analogs is that the light curve of σ Ori E is simpler

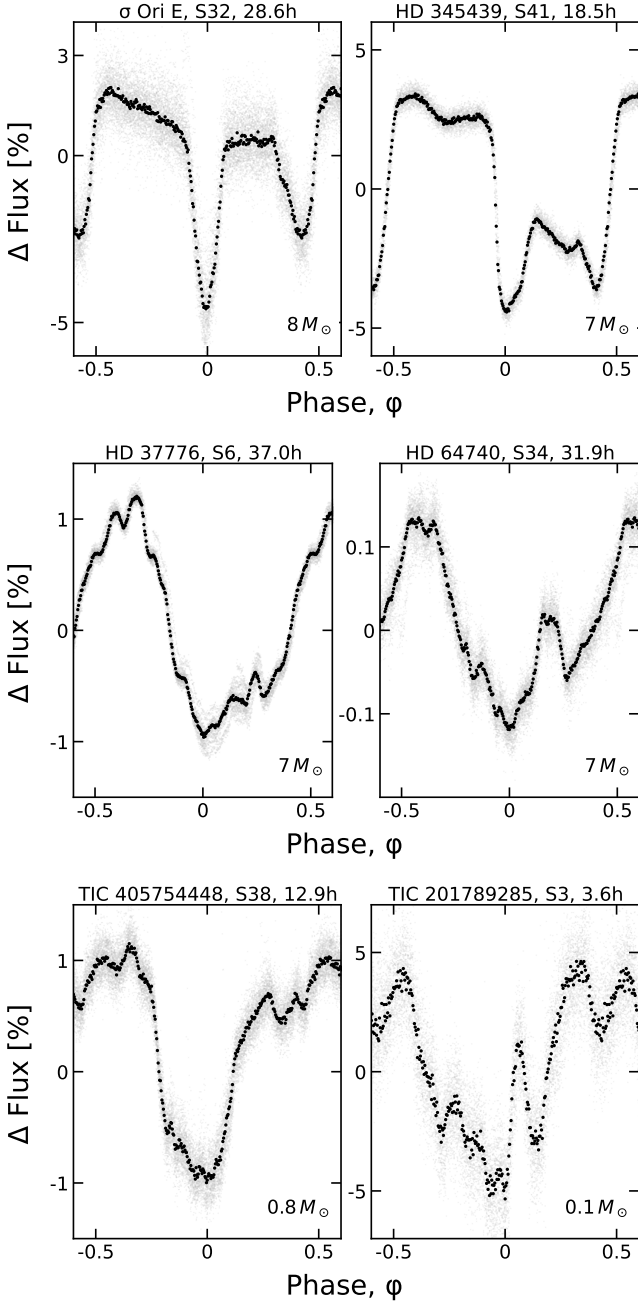


Figure 10. The magnetic B star connection. σ Ori E and HD 345439 (top row) are magnetic B stars with predominantly dipolar magnetic fields known to host circumstellar plasma tori. HD 37776 and HD 64740 (middle row) are analogous magnetic B stars with field topologies potentially dominated by high order multipoles. The bottom row compares the latter systems against the “best-matching” CPV light curves, selected by eye from Figure 4. CPVs have light curves that are visually similar to the topologically complex magnetic B stars. Stellar masses rounded to one significant figure are given in the lower right of each panel; the star, TESS sector, and period are listed in each subtitle.

than those in Figure 4, with only two broad local minima, and one “hump” (Figure 10; see also Jayaraman et al. 2022). Within the model proposed by Townsend et al., the simplicity of the light curve is the result of a simple dipolar magnetic field, which is typical of magnetic B stars (Aurière et al. 2007; Donati & Landstreet 2009). The magnetic axis needs to be tilted relative to the stellar spin axis in order to match the qualitative behavior of both the broadband light curves, and the line-profile variations seen in hydrogen, helium, and carbon (Oksala et al. 2012).

Two interesting and possibly telling exceptions to the rule that magnetic B stars have simple light curves are HD 37776 and HD 64740. HD 37776 is known from spectropolarimetry to have an extreme field geometry dominated by high order multipoles (Kochukhov et al. 2011). The field geometry of HD 64740, while potentially less extreme, also shows evidence for a non-dipolar contribution (Shultz et al. 2018). Recent TESS light curves of these two B stars appear surprisingly similar to the CPV light curves (Mikulášek et al. 2020). The middle row of Figure 10 shows the phased TESS light curves for these two stars, with by-eye best-matching CPVs shown underneath for comparison. The number of dips per cycle, the shapes of the dips, and the dip depths relative to the sinusoidal envelope are all similar. This connection suggests that the highly structured light curves of both the M dwarfs and the B stars are associated with (and perhaps caused by) strong non-dipolar magnetic fields. Non-dipolar fields for M dwarfs are plausible, given that Zeeman Doppler Imaging has revealed non-axisymmetric magnetic field patterns for the few M dwarfs for which this technique is technically feasible (see Kochukhov 2021, and references therein).

The physical similarity between the B stars and the M dwarfs could have its origin in the existence of a “centrifugal magnetosphere” (see Petit et al. 2013). In other words, both classes of objects might satisfy the condition $R_m > R_c$, for R_m the magnetosphere radius (sometimes called the Alfvén radius). Provided that charged particles are confined to move along magnetic field lines, material can then build up at the corotation radius (e.g. Romanova & Owocki 2015, Sec. 4, and references therein). In the converse “dynamical” case, when $R_m < R_c$, material interior to the magnetospheric radius returns to the stellar surface over the free-fall timescale. A simple estimate assuming a dipole field with $B_0 \approx 1\text{ kG}$ at the star’s surface, a local plasma number density $n \approx 10^9 \text{ cm}^{-3}$, and a plasma temperature 10^6 K gives magnetospheric radii of order a few times the corotation radii, R_c . This suggests that the existence of a centrifugal magnetosphere is plausible for young, rapidly rotating M dwarfs.

6. CONCLUSIONS

In this work, we searched 2-minute cadence TESS data collected from 2018 July to 2022 September for complex periodic variables (CPVs). The target stars were 65,760 late-K and early-to-mid M dwarfs within 150 pc and with TESS magnitudes $T < 16$. The selection function included $>80\%$ of such stars within 30 pc, and $<10\%$ of such stars at distances exceeding 100 pc (Figure 2).

We found 50 objects that showed complex quasiperiodic behavior over at least one TESS sector. These 50 bona fide CPVs are listed in Table 1. This table also includes 13 ambiguous CPVs, whose designation is less certain, and 3 impostors. We inferred ages for all but two of the 66 objects based on memberships in young stellar associations; we also derived temperatures and radii using SED fitting, and inferred stellar masses by interpolating against stellar evolutionary models. We caution that our sample is far from being volume-limited and is not even magnitude-limited: the TESS 2-minute stellar sample had a heterogeneous selection function which may have been biased in favor of young stars over field stars. Previous work however has shown that $\approx 1\text{-}3\%$ of M dwarfs younger than ≈ 100 Myr show the CPV phenomenon (Rebull et al. 2016; Günther et al. 2022; Rebull et al. 2022).

Analyzing the TESS light curves and stellar properties of our CPVs, we draw the following conclusions.

1. The sharpest CPV dips have durations of $\approx 0.05 P$ and depths of $\approx 1\text{-}3\%$ (Figures 4 and 6). Explaining dips this sharp requires material extrinsic to the stellar surface (see Section 1).
2. The shortest CPV dips, also with durations of $\approx 0.05 P$, match the expected transit duration for a small body at the corotation radius, $T_{\text{dur}} \equiv R_* P_{\text{rot}} / (\pi a)$ (see Section 4.2.2). Such dips are therefore likely produced by transits of bodies or distributions of optically-thick material that are smaller than the star.
3. Many CPV dips have durations a few times longer than T_{dur} (Figure 4). The dips are often superposed on a quasi-sinusoidal signal that presumably originates from starspots and faculae on the stellar surface. The only viable explanation currently known for sharp dips being superposed on the starspot signals is that concentrations (“clumps”) of circumstellar material corotate with the star. Assuming that the longer dips have the same physical origin as the shortest dips, the corotating clumps must also be capable of having sizes comparable to the star.
4. The mean periods of CPVs remain fixed to within a relative precision $\lesssim 0.1\%$ over the two-year ($\approx 1,000$ cycle) baseline of available observations. The light curve shapes always evolve over this timescale (Figure 6).
5. The dips in CPV light curves can have slightly different periods. LP 12-502, for instance, showed dips with four distinct periods within $\pm 0.3\%$ of its fundamental period, sometimes simultaneously, and each lasting for up to 50 cycles (Figure 9).
6. The CPV peaks and dips evolve over timescales that are both secular (≈ 100 cycles) and impulsive (< 1 cycle). Dip growth seems to happen over durations of at least ten cycles, and slow dip decay can also occur. “State-switches” correspond to dips collapsing instantaneously; they occur once every few months for both LP 12-502 and TIC 300651846. State-switches are almost always linked with observed optical flares. Such switches are suggestive

- of magnetic reconnection opening the “magnetic cage” that traps the dust.
7. The detailed morphology changes exhibited by LP 12-502 during its state-switches (e.g. Figure 8, cycles 1233-1264) imply that the flux dips are additive and independent.
8. The on-off duty cycle for CPVs is $\approx 75\%$, based on the fraction of bona fide CPVs that either turned on or turned off during TESS re-observations, two years after the initial observation (Figure 6).
9. The CPV phenomenon persists for $\gtrsim 150$ Myr, based on the existence of multiple CPVs in AB Dor, the Pleiades, and Psc-Eri (Section 2.3). It may even extend to 200 Myr, based on the one CPV we found in the Carina Near moving group (TIC 294328887; ≈ 200 Myr). The lack of detected CPVs in the Hyades and Praesepe suggests that the lifetime of the phenomenon is limited to the first few hundred million years.
10. Most CPVs are M dwarfs with masses $0.1\text{-}0.4 M_\odot$. Two sources, TIC 405754448 and TIC 405910546, have masses that appear to exceed $0.5 M_\odot$. Both are potentially binaries, and this may confuse our ability to accurately identify the source of the CPV signal (Section 3.4.2). We encourage additional scrutiny of these objects in future work.
11. The closest CPVs to the Sun are at distances of 15-20 pc; the brightest have $V \approx 12$ ($J \approx 7.5$). We have found most of the close exemplars in this work, since our CPV sample was $\gtrsim 80\%$ complete within 30 pc. The lack of CPVs in the volume-complete < 15 pc sample of $0.1\text{-}0.3 M_\odot$ stars analyzed by Winters et al. (2021) is consistent with this estimate. Expanding our analysis of the TESS data to the full frame images would yield a truly volume-limited selection function, and would expand the CPV census by about a factor of two within 50 pc, and by a factor of ten within 100 pc.
12. Surprising analogs to CPVs exist in two magnetic B stars, one of which is known to have an extreme multipolar field topology (Section 5.10). Since most magnetic B stars have dipolar magnetic fields, this suggests that the CPV dips and warps are similarly being sculpted by the stellar magnetic fields, and that the magnetic fields themselves are potentially also multipolar.
13. The rate of dip evolution can be used to place a model-dependent lower bound on how much material is either being accreted or ejected during the state changes (Section 5.8). Order of magnitude estimates require at least an asteroid belt’s worth of dust ($10^{-4} M_\oplus$) over 10^8 years, or at least $\approx 10^{-2} M_\oplus$ if the occulting material is gas.
- 1366 While many questions remain, two in particular will be important for clarifying what these objects might teach us in a broader astrophysical context: 1) Is the eclipsing material responsible for the phenomenon gas or dust? 2) What sets the characteristic clumping size for the circumstellar material?
- 1371 The distinction between gas or dust is important because it could clarify whether the CPV phenomenon is intrinsic, so that material comes from the star, or extrinsic, so that

it is sourced through some generic evolutionary phase of debris disks. This knowledge would in turn propagate to our understanding of whether the phenomenon is primarily teaching us about dust production and processing in gas-poor disks, or whether it is teaching us about the ability of cold gas to remain stable in hot stellar coronae for long durations. Observationally, acquisition of medium- or high-resolution time-series spectra holds a good chance at resolving the gas vs. dust question. Given our observed $\approx 75\%$ on-off duty cycles, such data must be acquired simultaneously with photometric time-series observations (e.g. during TESS re-observation) in order for detections and non-detections to be interpretable.

In both the gas and dust scenarios, CPVs are preferentially viewed edge-on. This implies that after correcting for the line-of-sight inclination, roughly one third of low mass stars (those that rotate rapidly enough; Günther et al. 2022) could trap circumstellar material in the same way. It also suggests that CPVs may preferentially show transiting planets at larger distances than the corotating material, though this conclusion would be dependent on whether the magnetic and stellar spin axes tend to be aligned. Given these points, observational follow-up work should include searching for outer transiting planets, and measuring equatorial velocities in order to test whether the stellar inclination angles are indeed preferentially edge-on. Any source of empirical information on the stellar magnetic field, whether from the Zeeman effect (e.g. Kochukhov 2021) or perhaps radio emission (e.g. Hallinan et al. 2015), could also help clarify the strength of the magnetospheres for these objects.

On the theoretical front, building a physical understanding of what sets the characteristic size scale of the clumping material would help clarify why the light curves have the bizarre shapes that are observed. The relevant puzzles in plasma physics and radiative transfer could perhaps be connected to our understanding of the close-in rocky planets that are expected to be present around most of these stars.

ACKNOWLEDGMENTS

LGB is grateful for support from the Heising-Simons 51 Pegasi b Fellowship, and for helpful conversations with J. Spake, A. Mann, G. Laughlin, and B. Draine. We are also grateful for the assistance of S. Yee, L. Weiss, H. Isaacson, and A. Howard in acquiring and reducing the HIRES spectra. This paper relied primarily on data collected by the TESS mission; the specific 2-minute cadence observations can be accessed via DOI [10.17909/t9-nmc8-f686](https://doi.org/10.17909/t9-nmc8-f686). Funding for the TESS mission is provided by NASA’s Science Mission Directorate. We thank the TESS Architects (G. Ricker, R. Vanderspek, D. Latham, S. Seager, and J. Jenkins) and the many TESS team members for their efforts to make the mission a continued success. LP 12-502 in particular was observed at 2-minute cadence thanks to the TESS Guest Investigator programs G022252 (PI: J. Schlieder; Sectors 18, 19, 25, 26) and G04168 (PI: R. Jayaraman; Sector 53). ADU acknowledges support by NASA under award number 80GSFC21M0002, as well as ROSES award 22-ADAP22-0070.

LGB conceived the project, performed the dip-counting search, light curve classification, cluster membership, SED, variability, and secondary-period analyses, and wrote the manuscript. RJ and SR performed the Fourier-based analysis and contributed to light curve classification. LR cross-examined the light curve classification, and contributed an independent SED analysis. ADU identified the magnetic B star connection. LAH contributed to project design. JNW, SR, and LAH significantly improved the clarity of the manuscript. GÁB acquired and maintained the servers used to run the dip-finding pipeline.

Software: `astrobase` (Bhatti et al. 2021), `astropy` (Astropy Collaboration et al. 2013, 2018, 2022), `lightkurve` (Lightkurve Collaboration et al. 2018), `numpy` (Harris et al. 2020), `pyGAM` (Servén & Brummitt 2018), `scipy` (Virtanen et al. 2020), `TESS-point` (Burke et al. 2020), `wotan` (Hippke et al. 2019).

Facilities: *Astrometry*: Gaia (Gaia Collaboration et al. 2018, 2023). *Imaging*: Second Generation Digitized Sky Survey. *Spectroscopy*: Keck:I (HIRES; Vogt et al. 1994). *Photometry*: TESS (Ricker et al. 2015), Broadband photometry: 2MASS (Skrutskie et al. 2006), APASS (Henden et al. 2016), Gaia (Gaia Collaboration et al. 2018, 2023), SDSS (York et al. 2000), WISE (Wright et al. 2010).

REFERENCES

- 1435 Alencar, S. H. P., Teixeira, P. S., Guimarães, M. M., et al. 2010, *A&A*, **519**, A88
- 1436 Allard, F., Homeier, D., & Freytag, B. 2012, *Philosophical Transactions of the Royal Society A: Mathematical, Physical and Engineering Sciences*, **370**, 2765
- 1437 Ansdel, M., Gaidos, E., Rappaport, S. A., et al. 2016, *ApJ*, **816**, 69
- 1441 Apai, D., Nardiello, D., & Bedin, L. R. 2021, *ApJ*, **906**, 64
- 1442 Asplund, M., Grevesse, N., Sauval, A. J., & Scott, P. 2009, *ARA&A*, **47**, 481
- 1444 Astropy Collaboration, Robitaille, T. P., Tollerud, E. J., et al. 2013, *A&A*, **558**, A33
- 1446 Astropy Collaboration, Price-Whelan, A. M., Sipőcz, B. M., et al. 2018, *AJ*, **156**, 123
- 1448 Astropy Collaboration, Price-Whelan, A. M., Lim, P. L., et al. 2022, *ApJ*, **935**, 167
- 1450 Aurière, M., Wade, G. A., Silvester, J., et al. 2007, *A&A*, **475**, 1053
- 1452 Bailer-Jones, C. A. L., Rybizki, J., Fouesneau, M., Demleitner, M., & Andrae, R. 2021, *AJ*, **161**, 147
- 1454 Baraffe, I., & Chabrier, G. 2018, *A&A*, **619**, A177
- 1455 Barber, R. J., Tennyson, J., Harris, G. J., & Tolchenov, R. N. 2006, *MNRAS*, **368**, 1087
- 1457 Basri, G. 2021, An Introduction to Stellar Magnetic Activity
- 1458 Bell, C. P. M., Mamajek, E. E., & Naylor, T. 2015, *MNRAS*, **454**, 593
- 1460 Berry, I. D., Owocki, S. P., Shultz, M. E., & ud-Doula, A. 2022, *MNRAS*, **511**, 4815
- 1462 Bhatti, W., Bouma, L., Joshua, et al. 2021, waqasbhatti/astrobase: astrobase v0.5.3, Zenodo
- 1464 Bodman, E. H. L., Quillen, A. C., Ansdel, M., et al. 2017, *MNRAS*, **470**, 202
- 1466 Bouma, L. G., Winn, J. N., Ricker, G. R., et al. 2020, *AJ*, **160**, 86
- 1467 Bouma, L. G., Curtis, J. L., Masuda, K., et al. 2022, *AJ*, **163**, 121
- 1468 Bressan, A., Marigo, P., Girardi, L., et al. 2012, *MNRAS*, **427**, 127
- 1469 Briceño, C., Calvet, N., Hernández, J., et al. 2019, *AJ*, **157**, 85
- 1470 Brogi, M., Keller, C. U., de Juan Ovelar, M., et al. 2012, *A&A*, **545**, L5
- 1472 Burke, C. J., Levine, A., Fausnaugh, M., et al. 2020, TESS-Point: High precision TESS pointing tool, Astrophysics Source Code Library, record ascl:2003.001
- 1475 Cantat-Gaudin, T., & Anders, F. 2020, *A&A*, **633**, A99
- 1476 Capistrant, B. K., Soares-Furtado, M., Vanderburg, A., et al. 2022, *ApJS*, **263**, 14
- 1478 Cardelli, J. A., Clayton, G. C., & Mathis, J. S. 1989, *ApJ*, **345**, 245
- 1479 Chen, Y., Girardi, L., Bressan, A., et al. 2014, *MNRAS*, **444**, 2525
- 1480 Christian, S., Vanderburg, A., Becker, J., et al. 2022, *AJ*, **163**, 207
- 1481 Cody, A. M., & Hillenbrand, L. A. 2010, *ApJS*, **191**, 389
- 1482 Cody, A. M., Stauffer, J., Baglin, A., et al. 2014, *AJ*, **147**, 82
- 1483 Collier Cameron, A. 1999, in Astronomical Society of the Pacific Conference Series, Vol. 158, Solar and Stellar Activity: Similarities and Differences, ed. C. J. Butler & J. G. Doyle, 146
- 1486 Collier Cameron, A., Duncan, D. K., Ehrenfreund, P., et al. 1990, *MNRAS*, **247**, 415
- 1488 Collier Cameron, A., & Robinson, R. D. 1989, *MNRAS*, **238**, 657
- 1489 Curtis, J. L., Agüeros, M. A., Mamajek, E. E., Wright, J. T., & Cummings, J. D. 2019, *AJ*, **158**, 77
- 1491 Dahm, S. E. 2015, *ApJ*, **813**, 108
- 1492 David, T. J., & Hillenbrand, L. A. 2015, *ApJ*, **804**, 146
- 1493 Donati, J. F., & Landstreet, J. D. 2009, *ARA&A*, **47**, 333
- 1494 Draine, B. T. 1985, *ApJS*, **57**, 587
- 1495 Dressing, C. D., & Charbonneau, D. 2015, *ApJ*, **807**, 45
- 1496 Dunstone, N. J., Barnes, J. R., Collier Cameron, A., & Jardine, M. 2006, *MNRAS*, **365**, 530
- 1498 Farihi, J., von Hippel, T., & Pringle, J. E. 2017, *MNRAS*, **471**, L145
- 1500 Fausnaugh, M., Morgan, E., Vanderspek, R., et al. 2021, *PASP*, **133**, 095002
- 1502 Feiden, G. A. 2016, *A&A*, **593**, A99
- 1503 Ferreira, J. M. 2000, *MNRAS*, **316**, 647
- 1504 Gagné, J., Mamajek, E. E., Malo, L., et al. 2018, *ApJ*, **856**, 23
- 1505 Gaia Collaboration, Brown, A. G. A., Vallenari, A., et al. 2018, *A&A*, **616**, A1
- 1507 Gaia Collaboration, Smart, R. L., Sarro, L. M., et al. 2021, *A&A*, **649**, A6
- 1509 Gaia Collaboration, Vallenari, A., Brown, A. G. A., et al. 2023, *A&A*, **674**, A1
- 1511 Gaidos, E., Jacobs, T., LaCourse, D., et al. 2019, *MNRAS*, **488**, 4465
- 1513 Gaidos, E., Mann, A. W., Rojas-Ayala, B., et al. 2022, *MNRAS*, **514**, 1386
- 1515 Gilbert, E. A., Barclay, T., Quintana, E. V., et al. 2022, *AJ*, **163**, 147
- 1517 Gray, D. F. 1992, The observation and analysis of stellar photospheres., Vol. 20
- 1519 Gully-Santiago, M. A., Herczeg, G. J., Czekala, I., et al. 2017, *ApJ*, **836**, 200
- 1521 Günther, M. N., Berardo, D. A., Ducrot, E., et al. 2022, *AJ*, **163**, 144
- 1523 Hallinan, G., Littlefair, S. P., Cotter, G., et al. 2015, *Nature*, **523**, 568
- 1525 Harris, C. R., Millman, K. J., van der Walt, S. J., et al. 2020, *Nature*, **585**, 357
- 1527 Henden, A. A., Templeton, M., Terrell, D., et al. 2016, VizieR Online Data Catalog, II/336
- 1529 Hesser, J. E., Ugarte, P. P., & Moreno, H. 1977, *ApJL*, **216**, L31
- 1530 Hippke, M., David, T. J., Mulders, G. D., & Heller, R. 2019, *AJ*, **158**, 143

- 1532 Howard, A. W., Johnson, J. A., Marcy, G. W., et al. 2010, *ApJ*,
1533 **721, 1467**
- 1534 Howell, S. B., Sobeck, C., Haas, M., et al. 2014, *PASP*, **126**, 398
- 1535 Izidoro, A., & Raymond, S. N. 2018, in *Handbook of Exoplanets*,
1536 ed. H. J. Deeg & J. A. Belmonte, 142
- 1537 Jardine, M., & Collier Cameron, A. 2019, *MNRAS*, **482**, 2853
- 1538 Jayaraman, R., Hubrig, S., Holdsworth, D. L., et al. 2022, *ApJL*,
1539 **924, L10**
- 1540 Jeffries, R. D. 1993, *MNRAS*, **262**, 369
- 1541 Jenkins, J. M., Twicken, J. D., McCauliff, S., et al. 2016, in *Society
1542 of Photo-Optical Instrumentation Engineers (SPIE) Conference
1543 Series, Vol. 9913, Software and Cyberinfrastructure for
1544 Astronomy IV*, ed. G. Chiozzi & J. C. Guzman, 99133E
- 1545 Johns-Krull, C. M., Prato, L., McLane, J. N., et al. 2016, *ApJ*, **830**,
1546 **15**
- 1547 Justesen, A. B., & Albrecht, S. 2021, *ApJ*, **912**, 123
- 1548 Kenyon, S. J., & Hartmann, L. 1995, *ApJS*, **101**, 117
- 1549 Kerr, R. M. P., Rizzuto, A. C., Kraus, A. L., & Offner, S. S. R.
1550 2021, *ApJ*, **917**, 23
- 1551 Kochukhov, O. 2021, *A&A Rv*, **29**, 1
- 1552 Kochukhov, O., Lundin, A., Romanyuk, I., & Kudryavtsev, D.
1553 2011, *ApJ*, **726**, 24
- 1554 Koen, C. 2021, *MNRAS*, **500**, 1366
- 1555 —. 2023, *MNRAS*, **518**, 2921
- 1556 Königl, A. 1991, *ApJL*, **370**, L39
- 1557 Lamb, F. K., Pethick, C. J., & Pines, D. 1973, *ApJ*, **184**, 271
- 1558 Landstreet, J. D., & Borra, E. F. 1978, *ApJL*, **224**, L5
- 1559 Leitzinger, M., Odert, P., Zaqrashvili, T. V., et al. 2016, *MNRAS*,
1560 **463**, 965
- 1561 Li, R., Chen, Y.-X., & Lin, D. N. C. 2022, *MNRAS*, **510**, 5246
- 1562 Lightkurve Collaboration, Cardoso, J. V. d. M., Hedges, C., et al.
1563 2018, *Lightkurve: Kepler and TESS time series analysis in
1564 Python*, Astrophysics Source Code Library, record ascl:1812.013
- 1565 Long, M., Romanova, M. M., & Lovelace, R. V. E. 2005, *ApJ*, **634**,
1566 **1214**
- 1567 MacLeod, M., & Oklopčić, A. 2022, *ApJ*, **926**, 226
- 1568 McCann, J., Murray-Clay, R. A., Kratter, K., & Krumholz, M. R.
1569 2019, *ApJ*, **873**, 89
- 1570 Mikulášek, Z., Krtička, J., Shultz, M. E., et al. 2020, in *Stellar
1571 Magnetism: A Workshop in Honour of the Career and
1572 Contributions of John D. Landstreet*, ed. G. Wade, E. Alecian,
1573 D. Bohlender, & A. Sigut, Vol. 11, 46
- 1574 Murphy, S. J., Lawson, W. A., & Bessell, M. S. 2013, *MNRAS*,
1575 **435**, 1325
- 1576 Nakajima, R. 1985, *Ap&SS*, **116**, 285
- 1577 Oksala, M. E., Wade, G. A., Townsend, R. H. D., et al. 2012,
1578 *MNRAS*, **419**, 959
- 1579 Onitsuka, M., Fukui, A., Narita, N., et al. 2017, *PASJ*, **69**, L2
- 1580 Paegert, M., Stassun, K. G., Collins, K. A., et al. 2021, *arXiv
1581 e-prints*, arXiv:2108.04778
- 1582 Palumbo, E. K., Montet, B. T., Feinstein, A. D., et al. 2022, *ApJ*,
1583 **925**, 75
- 1584 Park, R. S., Vaughan, A. T., Konopliv, A. S., et al. 2019, *Icarus*,
1585 **319**, 812
- 1586 Pecaut, M. J., & Mamajek, E. E. 2016, *MNRAS*, **461**, 794
- 1587 Penoyre, Z., Belokurov, V., & Evans, N. W. 2022, *MNRAS*, **513**,
1588 **5270**
- 1589 Pérez Paolino, F., Bary, J. S., Petersen, M. S., et al. 2023, *ApJ*, **946**,
1590 **10**
- 1591 Petit, V., Owocki, S. P., Wade, G. A., et al. 2013, *MNRAS*, **429**,
1592 **398**
- 1593 Popinchalk, M., Faherty, J. K., Curtis, J. L., et al. 2023, *ApJ*, **945**,
1594 **114**
- 1595 Pribulla, T., Borkovits, T., Jayaraman, R., et al. 2023, *MNRAS*,
1596 **524**, 4220
- 1597 Rajpurohit, A. S., Reylé, C., Allard, F., et al. 2013, *A&A*, **556**, A15
- 1598 Rappaport, S., Barclay, T., DeVore, J., et al. 2014, *ApJ*, **784**, 40
- 1599 Rappaport, S., Levine, A., Chiang, E., et al. 2012, *ApJ*, **752**, 1
- 1600 Rappaport, S., Vanderburg, A., Jacobs, T., et al. 2018, *MNRAS*,
1601 **474**, 1453
- 1602 Ratzenböck, S., Meingast, S., Alves, J., Möller, T., & Bomze, I.
1603 2020, *A&A*, **639**, A64
- 1604 Rebull, L. M., Stauffer, J. R., Cody, A. M., et al. 2018, *AJ*, **155**,
1605 **196**
- 1606 Rebull, L. M., Stauffer, J. R., Hillenbrand, L. A., et al. 2022, *AJ*,
1607 **164**, 80
- 1608 Rebull, L. M., Stauffer, J. R., Bouvier, J., et al. 2016, *AJ*, **152**, 114
- 1609 Reinhold, T., Bell, K. J., Kuszlewicz, J., Hekker, S., & Shapiro,
1610 A. I. 2019, *A&A*, **621**, A21
- 1611 Ricker, G. R., Winn, J. N., Vanderspek, R., et al. 2015, *Journal of
1612 Astronomical Telescopes, Instruments, and Systems*, **1**, 014003
- 1613 Rivinius, T., Carciofi, A. C., & Martayan, C. 2013, *A&A Rv*, **21**,
1614 **69**
- 1615 Rizzuto, A. C., Newton, E. R., Mann, A. W., et al. 2020, *AJ*, **160**,
1616 **33**
- 1617 Robinson, C. E., Espaillat, C. C., & Owen, J. E. 2021, *ApJ*, **908**, 16
- 1618 Rodriguez, D. R., van der Plas, G., Kastner, J. H., et al. 2015,
1619 *A&A*, **582**, L5
- 1620 Romanova, M. M., & Owocki, S. P. 2015, *SSRv*, **191**, 339
- 1621 Sanchis-Ojeda, R., Rappaport, S., Pallè, E., et al. 2015, *ApJ*, **812**,
1622 **112**
- 1623 Sanderson, H., Jardine, M., Collier Cameron, A., Morin, J., &
1624 Donati, J. F. 2023, *MNRAS*, **518**, 4734
- 1625 Saur, J., Neubauer, F. M., Connerney, J. E. P., Zarka, P., &
1626 Kivelson, M. G. 2004, in *Jupiter. The Planet, Satellites and
1627 Magnetosphere*, ed. F. Bagenal, T. E. Dowling, & W. B.
1628 McKinnon, Vol. 1, 537
- 1629 Servén, D., & Brummitt, C. 2018, *pyGAM: Generalized Additive
1630 Models in Python*

- 1631 Shultz, M. E., Wade, G. A., Rivinius, T., et al. 2018, [MNRAS](#), **475**,
1632 **5144**
- 1633 Skrutskie, M. F., Cutri, R. M., Stiening, R., et al. 2006, [AJ](#), **131**,
1634 **1163**
- 1635 Smith, J. C., Stumpe, M. C., Jenkins, J. M., et al. 2017, Kepler
1636 Data Processing Handbook: Presearch Data Conditioning,
1637 Kepler Science Document KSCI-19081-002, id. 8. Edited by Jon
1638 M. Jenkins.
- 1639 Somers, G., Cao, L., & Pinsonneault, M. H. 2020, [ApJ](#), **891**, 29
- 1640 Speagle, J. S. 2020, [MNRAS](#), **493**, 3132
- 1641 Stassun, K. G., Kratter, K. M., Scholz, A., & Dupuy, T. J. 2012,
[ApJ](#), **756**, 47
- 1642 Stassun, K. G., Oelkers, R. J., Paegert, M., et al. 2019, [AJ](#), **158**, 138
- 1643 Stauffer, J., Rebull, L. M., Cody, A. M., et al. 2018a, [AJ](#), **156**, 275
- 1644 Stauffer, J., Collier Cameron, A., Jardine, M., et al. 2017, [AJ](#), **153**,
1645 **152**
- 1646 Stauffer, J., Rebull, L., David, T. J., et al. 2018b, [AJ](#), **155**, 63
- 1647 Stauffer, J., Rebull, L. M., Jardine, M., et al. 2021, [AJ](#), **161**, 60
- 1648 Stellingwerf, R. F. 1978, [ApJ](#), **224**, 953
- 1649 Tokovinin, A., & Briceño, C. 2018, [AJ](#), **156**, 138
- 1650 Townsend, R. H. D., & Owocki, S. P. 2005, [MNRAS](#), **357**, 251
- 1651 Townsend, R. H. D., Owocki, S. P., & Groote, D. 2005, [ApJL](#), **630**,
1652 **L81**
- 1653 Vanderburg, A., Johnson, J. A., Rappaport, S., et al. 2015, [Nature](#),
1654 **526**, 546
- 1655 Vial, J.-C., & Engvold, O. 2015, *Astrophysics and Space Science
Library*, Vol. 415, Solar Prominences
- 1656 Vines, J. I., & Jenkins, J. S. 2022, [MNRAS](#), **513**, 2719
- 1657 Virtanen, P., Gommers, R., Oliphant, T. E., et al. 2020, [Nature
Methods](#), **17**, 261
- 1658 Vogt, S. S., Allen, S. L., Bigelow, B. C., et al. 1994, in *Society of
Photo-Optical Instrumentation Engineers (SPIE) Conference Series*, Vol. 2198, *Instrumentation in Astronomy VIII*, ed. D. L.
1659 Crawford & E. R. Craine, 362
- 1660 Vos, J. M., Faherty, J. K., Gagné, J., et al. 2022, [ApJ](#), **924**, 68
- 1661 Wade, G. A., Petit, V., Grunhut, J. H., Neiner, C., & MiMeS
1662 Collaboration. 2016, in *Astronomical Society of the Pacific
Conference Series*, Vol. 506, *Bright Emissaries: Be Stars as
Messengers of Star-Disk Physics*, ed. T. A. A. Sigut & C. E.
1663 Jones, 207
- 1664 Waugh, R. F. P., & Jardine, M. M. 2022, [MNRAS](#), **514**, 5465
- 1665 Winters, J. G., Charbonneau, D., Henry, T. J., et al. 2021, [AJ](#), **161**,
1666 **63**
- 1667 Winters, J. G., Henry, T. J., Jao, W.-C., et al. 2019, [AJ](#), **157**, 216
- 1668 Wright, E. L., Eisenhardt, P. R. M., Mainzer, A. K., et al. 2010, [AJ](#),
1669 **140**, 1868
- 1670 York, D. G., Adelman, J., Anderson, John E., J., et al. 2000, [AJ](#),
1671 **120**, 1579
- 1672 Zhan, Z., Günther, M. N., Rappaport, S., et al. 2019, [ApJ](#), **876**, 127
- 1673 Zieba, S., Zwintz, K., Kenworthy, M. A., & Kennedy, G. M. 2019,
[A&A](#), **625**, L13
- 1674 Zuckerman, B. 2019, [ApJ](#), **870**, 27
- 1675 Zuckerman, B., Bessell, M. S., Song, I., & Kim, S. 2006, [ApJL](#),
1676 **649**, L115

Table 1. Bona fide, candidate, and debunked complex periodic variables from the TESS 2-minute data. The non-truncated machine readable versions are accessible both through the online journal, and at <https://zenodo.org/record/8327508>.

TIC	<i>T</i>	<i>d</i>	$G_{\text{BP}} - G_{\text{RP}}$	RUWE	<i>P</i>	Assoc	Age	T_{eff}	R_*	M_*	R_c	P_{sec}	Quality	Bin	N_{sector}
–	mag	pc	mag	–	hr	–	Myr	K	R_\odot	M_\odot	R_*	hr	–	–	–
368129164	9.29	18.3	2.89	6.95	6.44	ABDMG	149	3140	0.71	0.4	1.81	2.60	1	011	3
405754448	9.63	92.6	1.75	6.81	12.92	LCC	15	4273	1.5	0.82	1.74	134.4	1	011	5
167664935	10.31	62.5	2.52	5.05	14.05	UCL	16	3325	1.42	0.38	1.5	10.71	1	011	3
311092148	11.03	26.8	3.03	1.5	7.86	COL	42	3035	0.5	0.27	2.6	–	1	000	1
402980664	11.11	21.3	3.04	1.48	18.56	COL	42	3080	0.37	0.22	5.76	–	1	000	10
50745567	11.28	38.0	3.22	3.95	6.34	BPMG	24	3014	0.67	0.28	1.68	28.55	1	011	2
59836633	11.38	61.9	2.71	1.21	14.96	BPMG	24	3282	0.82	0.48	2.91	–	1	000	3
425933644	11.4	43.2	2.82	10.29	11.67	THA	45	3151	0.63	0.4	3.06	–	1	010	6
142173958	11.61	70.6	3.09	2.9	11.76	TWA	10	3028	1.15	0.26	1.45	12.84	1	011	3
146539195	11.62	48.2	3.37	2.86	6.73	BPMG	24	2898	0.8	0.24	1.38	7.29	1	011	2
206544316	11.63	42.8	2.89	1.26	7.73	THA	45	3114	0.57	0.35	2.44	–	1	000	6
335598085	11.9	105.5	2.85	2.79	15.85	LCC	15	3119	1.34	0.28	1.56	17.94	1	011	3
405910546	12.11	111.9	2.36	1.09	37.99	LCC	15	3455	0.92	0.6	5.26	–	1	100	4
272248916	12.15	80.5	2.83	5.5	8.9	UCL	16	3193	0.81	0.4	1.97	50.7	1	011	3
178155030	12.17	46.8	2.91	1.29	11.67	THA	45	3097	0.49	0.3	3.53	–	1	000	4
224283342	12.29	38.0	3.04	1.27	21.3	COL	42	3050	0.39	0.22	6.08	–	1	100	3
89026133	12.31	131.6	2.82	4.0	11.2	UCL	16	3188	1.33	0.31	1.29	27.83	1	011	3
234295610	12.51	48.1	3.04	1.13	18.29	THA	45	3074	0.44	0.27	5.09	–	1	000	3
118449916	12.54	97.1	3.09	25.18	12.31	TAU	2	3025	1.04	0.28	1.7	6.71	1	011	4
67897871	12.55	148.2	3.01	2.55	6.23	USCO	10	3082	1.5	0.18	0.65	6.72	1	011	2
353730181	12.65	106.6	2.75	1.23	13.51	TAU	2	3253	0.8	0.41	2.65	–	1	000	4
201898222	12.68	42.2	3.21	1.29	10.7	THA	45	2996	0.39	0.2	3.69	13.62	1	001	5
264767454	12.73	123.3	2.93	12.3	10.01	COL(?)	42	3150	1.0	0.42	1.76	20.62	1	011	13
442571495	12.75	80.8	3.03	1.64	9.59	UCL	16	3099	0.65	0.3	2.35	13.82	1	001	3
2234692	12.8	53.7	3.0	1.2	6.52	COL	42	3098	0.44	0.26	2.56	59.8	1	001	7
94088626	12.88	57.6	3.07	1.12	6.6	ARG	45	3090	0.46	0.27	2.53	–	1	000	2
264599508	12.88	79.7	3.01	1.89	7.9	COL	42	3098	0.62	0.4	2.4	8.99	1	001	7
363963079	12.92	83.1	3.09	8.0	7.82	ARG	45	3040	0.67	0.4	2.21	7.41	1	011	7
193831684	13.03	51.6	3.23	1.16	31.02	BPMG	24	2971	0.42	0.2	6.87	–	1	000	3
177309964	13.1	91.0	2.94	1.15	10.88	CAR	45	3125	0.62	0.4	2.95	–	1	000	34
425937691	13.18	43.1	3.77	2.86	4.82	THA	45	2782	0.41	0.16	1.91	3.22	1	011	5
141146667	13.28	57.6	3.28	1.23	3.93	FIELD	NaN	2968	0.42	NaN	NaN	–	1	000	6
332517282	13.29	39.0	3.27	1.05	9.67	ABDMG	149	2975	0.28	0.2	4.87	–	1	000	3
144486786	13.3	77.4	3.05	15.05	6.82	COL	42	3074	0.51	0.3	2.38	11.49	1	011	4
38820496	13.3	44.1	3.37	1.08	15.73	THA	45	2903	0.34	0.16	5.13	–	1	000	5
289840926	13.31	40.2	3.75	1.16	4.8	BPMG	24	2807	0.36	0.14	2.05	15.64	1	001	3
404144841	13.33	77.1	3.19	1.11	10.74	TWA	10	3008	0.52	0.22	2.86	–	1	000	4
89463560	13.45	123.9	2.97	1.31	9.43	ARG	45	3055	0.75	0.37	2.15	7.76	1	001	10
300651846	13.49	109.2	2.86	1.16	8.26	CAR	45	3136	0.62	0.4	2.44	–	1	000	31
267953787	13.49	130.5	3.59	1.2	17.46	TAU	2	2826	1.06	0.12	1.59	–	1	000	4
68812630	13.6	123.8	3.22	1.63	9.04	TAU	2	2996	0.76	0.27	1.86	5.28	1	001	3
141306513	13.65	50.2	3.4	1.08	13.36	THA	45	2964	0.32	0.16	4.85	–	1	000	2
201789285	14.03	45.4	3.82	1.19	3.64	THA	45	2757	0.3	0.12	2.02	–	1	000	5
294328887	14.23	97.1	3.22	1.05	8.51	CARN	200	2994	0.45	0.35	3.33	–	1	000	35

Table 1 *continued*

Table 1 (*continued*)

312410638	14.3	136.9	3.12	1.09	28.06	UCL	16	3030	0.58	0.25	5.11	-	1	000	3
38539720	14.52	129.4	3.37	1.2	9.16	PERI	120	2924	0.57	0.25	2.43	-	1	000	1
359892714	14.53	95.5	4.04	1.07	11.33	EPSC	3	2675	0.55	0.13	2.36	-	1	000	6
118769116	14.58	119.0	3.6	1.13	8.56	TAU	2	2852	0.56	0.2	2.18	-	1	000	4
440725886	14.69	135.1	2.96	1.06	3.92	PLE	112	3109	0.45	0.35	1.99	-	1	000	5
397791443	15.01	151.1	3.1	1.06	6.95	IC2602	46	3031	0.48	0.26	2.46	-	1	000	6
160329609	9.65	8.7	3.4	1.18	24.31	ARG	45	2912	0.35	0.16	6.6	-	0	000	3
148646689	12.14	140.4	2.44	1.7	10.63	UCL	16	3466	1.25	0.55	1.61	13.37	0	001	3
280945693	12.27	98.2	2.97	1.16	15.27	LCC	15	3103	1.09	0.31	1.94	-	0	100	5
165184400	12.37	43.2	3.02	1.24	15.91	THA	45	3076	0.42	0.25	4.74	-	0	000	4
245834739	12.55	115.4	2.85	1.49	10.47	TAU	2	3112	1.02	0.36	1.68	9.86	0	001	6
125843782	13.01	127.7	2.86	1.21	44.17	TAU	2	3135	0.9	0.35	4.97	-	0	000	4
244161191	13.17	44.7	3.54	1.28	7.17	COL	42	2860	0.38	0.18	2.8	8.39	0	001	3
231058925	13.17	51.2	3.25	1.35	8.87	THA	45	2978	0.38	0.2	3.33	-	0	000	5
301676454	13.4	70.7	3.07	1.24	9.18	ARG	45	3009	0.47	0.25	2.96	-	0	000	1
58084670	13.58	140.2	2.82	1.06	11.16	FIELD	NaN	3138	0.77	NaN	NaN	-	0	000	6
67745212	13.63	27.8	3.8	1.11	5.12	COL	42	2781	0.21	0.09	3.17	-	0	000	2
5714469	13.73	78.3	3.65	1.12	10.35	UCL	16	2828	0.54	0.18	2.53	-	0	000	3
259586708	13.82	95.6	2.93	1.17	22.52	COL	42	3133	0.46	0.29	5.84	-	0	000	7
435903839	11.95	80.7	2.49	17.7	10.82	ABDMG(?)	149	3458	0.76	0.54	2.66	-	-1	010	6
57830249	11.96	48.8	3.2	1.34	43.82	TWA	10	2948	0.7	0.25	5.63	-	-1	000	3
193136669	13.06	61.1	3.49	1.22	37.64	TWA	10	2855	0.58	0.19	5.62	-	-1	000	4

NOTE—This table includes 50 good CPVs (Quality flag 1), 13 ambiguous CPVs (Quality flag 0), and 3 impostors (Quality flag -1). The three-bit binarity flag “Bin” is for Gaia DR3 `radial_velocity_error` outliers (bit 1), Gaia DR3 `ruwe` outliers (bit 2), and stars with multiple TESS periods (bit 3). The machine-readable version, available online, includes additional columns for the Gaia DR2 and DR3 source identifiers, as well as the stellar parameter uncertainties. The age uncertainties are typically $\approx \pm 10\%$, but can be asymmetric. The median statistical uncertainties on the temperature, radius, and mass are $\pm 50\text{ K}$, $\pm 4\%$ and $\pm 9\%$ respectively. N_{sector} denotes the number of TESS sectors for which *any* data are expected to be acquired between 2018 July and 2024 Oct. This number is generally greater than the number of sectors for which 2-minute cadence data exist. Association names and provenance follow conventions adopted by Gagné et al. (2018): ABDMG: AB Doradus moving group (Bell et al. 2015). ARG: Argus (Zuckerman 2019). BPMG: β Pic moving group (Bell et al. 2015). CARN: Carina Near moving group (Zuckerman et al. 2006). COL: Columba (Bell et al. 2015). EPSC: ϵ Chamæleonis (Murphy et al. 2013). LCC: Lower Centaurus Crux (Pecaut & Mamajek 2016). PERI: Pisces-Eridani (Curtis et al. 2019). PLE: Pleiades (Dahm 2015). TAU: Taurus (Kenyon & Hartmann 1995). THA: Tucana-Horologium association (Bell et al. 2015). TWA: TW Hydriæ association (Bell et al. 2015). UCL: Upper Centaurus Lupus (Pecaut & Mamajek 2016). USCO: Upper Scorpius (Pecaut & Mamajek 2016). The “(?)” string denotes low-confidence membership.

APPENDIX

A. THE RING HYPOTHESIS

One hypothesis for the CPVs, presented by Zhan et al. (2019), is that the star might be “*orbited by one or more rings composed of dust-size or somewhat larger particles... The ring particles would move in Keplerian orbits at relatively large distances from the star, and therefore the sublimation lifetime would not be an issue even if the particles are dust-like in size.*” A sketch of this scenario was presented by Zhan et al. (2019), in their Figure 11. An example set of proposed parameters involved a ring inclined with respect to the stellar spin axis by a few degrees, and with inner and outer radii of 10 and 15 stellar radii.

One concern with the ring hypothesis is that if a cool spot were to transit behind the ring, it would produce a brightening, not a dimming. Most CPVs show dimmings. The ring scenario would therefore imply that large hot spots are common in the photospheres of pre-main-sequence M dwarfs. Empirical evidence however suggests that cool spots dominate the optical variability of disk-free pre-main-sequence stars. This evidence includes flux excursions caused by spot-crossings during planetary transits (e.g. Rizzuto et al. 2020; Gilbert et al. 2022), correlations between simultaneous photometric and chromospheric time-series (Reinhold et al. 2019), and stellar spectra that show molecules that only form at cool temperatures (e.g. Gully-Santiago et al. 2017; Pérez Paolino et al. 2023).

An independent concern with the ring hypothesis is that it is fine-tuned. The model requires specific locations for the inner edge and the outer edge of the ring, an inclination that yields a band with a specific apparent size, and material in the ring that must be optically thick while also being homogeneous enough to not induce any apparent photometric variability. It is challenging

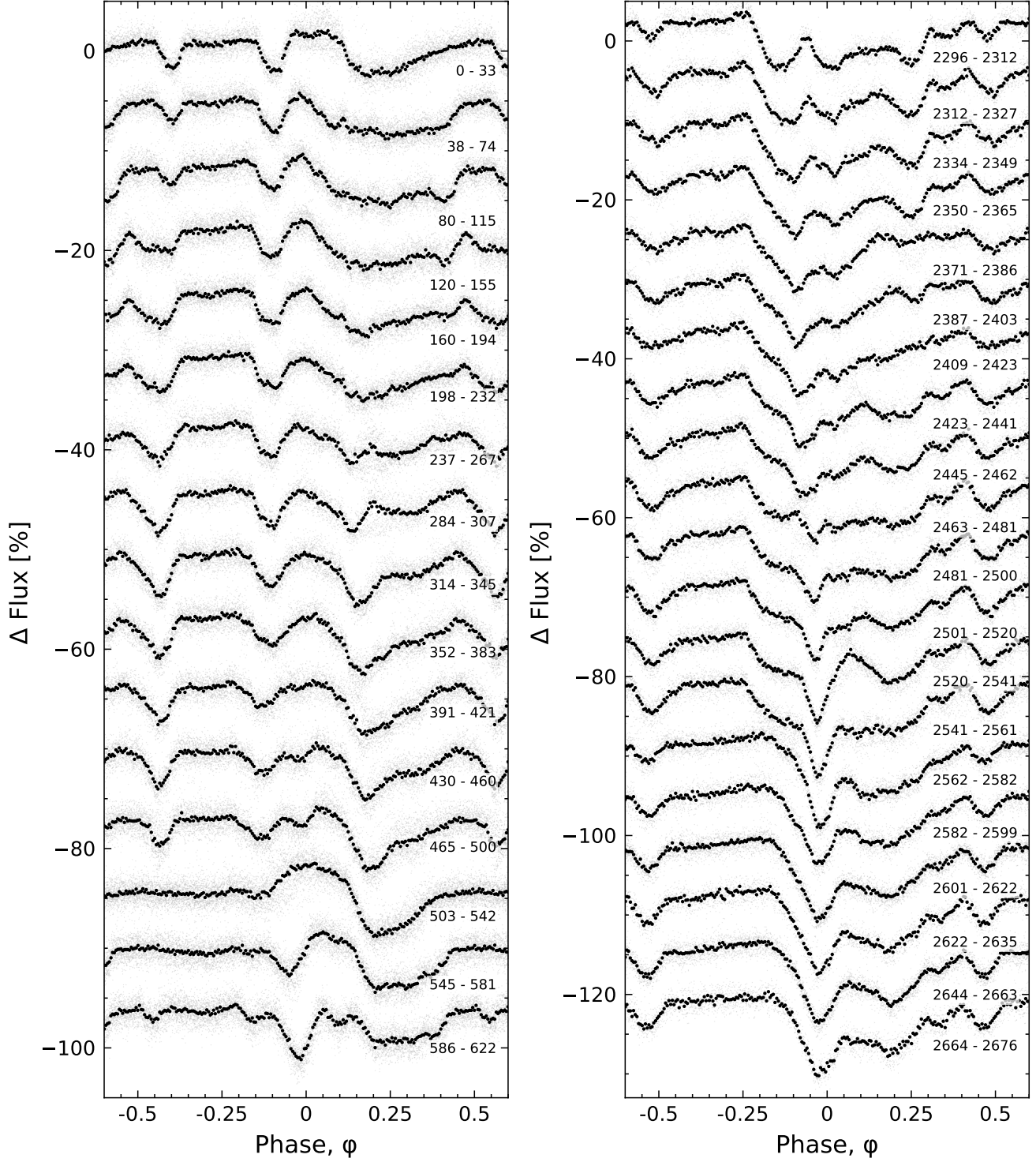


Figure 11. Light curve evolution of TIC 300651846. All available 2-minute cadence data as of 2023 Aug 11 are shown. Cycles 0 to 622 span TESS Sectors 32-39 (Nov 2020–June 2021); cycles 2296-2676 span Sectors 61-65 (Jan–June 2023). We assumed a 8.254 hr period and a fixed reference epoch (BTJD 2174.127) for both panels. Light curve segments are split based on the presence of gaps longer than three hours. Cycle numbers are listed in the lower-right of each light curve segment.

1702 to ascribe specific probabilities to any one of these factors. However the requirement that they all be simultaneously met seems
 1703 sufficiently severe to disfavor this scenario.

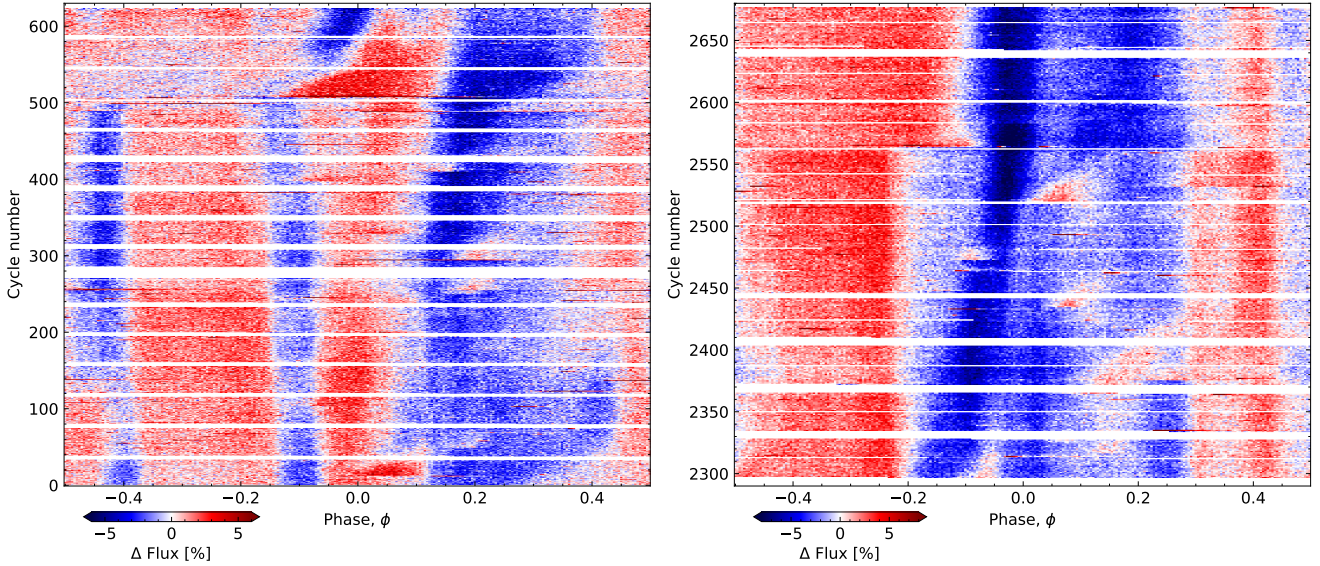


Figure 12. River plots of TIC 300651846. This is an alternative visualization of the data in Figure 11. All available 2-minute cadence data as of 2023 Aug 11 are shown. Cycles 0 to 622 span TESS Sectors 32-39 (Nov 2020–June 2021); cycles 2296–2676 span Sectors 61-65 (Jan–June 2023). We assumed $P=8.254$ hr and $t_0=2174.127$ [BTJD]. Note that the two panels have slightly different color scales.

1704

B. TIC 300651846

1705 Figures 11 and 12 show 2-minute cadence data for TIC 300651846, a CPV in the TESS continuous viewing zone. If it were
 1706 not for the existence of LP 12-502, this source would have received greater attention. With the exception of a few sectors, TESS
 1707 data will exist for TIC 300651846 for at least Sectors 1-12, 27-39, and 61-69. While most of the available data exist in the full
 1708 frame images, Figures 11 and 12 focus only on the currently available 2-minute cadence data.

1709 During Sectors 32-39, the source shows between one and four local minima per cycle. During the early portions of Sectors
 1710 61-65, it is more complex, with at least five clear local minima per cycle. As the source evolves, its shape becomes simpler, and
 1711 the sharpness of one global minimum appears to increase.

1712 State-switches analogous to those observed in LP 12-502 occur at cycles 498 and 2554. During the cycle 498 switch, two
 1713 narrow dips at $\phi \approx -0.4$ and $\phi \approx 0.0$ collapse. For the cycle 2554 switch, a longer dip collapses. This is visible as a change
 1714 in curvature in Figure 11 between $\phi \in [-0.25, -0.05]$ across cycles 2520-2561. The more typical dip evolution timescales for
 1715 TIC 300651846 seem to be ≈ 50 -100 cycles. Unlike the LP 12-502 river plots (Figure 9), we did not subtract any “continuum
 1716 sinusoid” for this source, because the continuum is not as obviously defined.

1717

C. LITERATURE COMPARISON

1718 We compared our CPV search results against previous work by compiling a list of CPVs from both K2 (Stauffer et al. 2017,
 1719 2018b) and TESS (Zhan et al. 2019; Bouma et al. 2020; Stauffer et al. 2021; Günther et al. 2022; Popinchalk et al. 2023). We
 1720 counted PTFO 8-8695 as a TESS-detected CPV (but see Bouma et al. 2020, and references therein). This effort resulted in a list
 1721 of 74 unique objects that had been reported to be CPVs. We made no attempt to reclassify these sources based on our subjective
 1722 grading scheme. TESS contributed 41 of the 74 objects; the remaining 33 were from K2.

1723 *How many known CPVs did we miss?*—A minority of the literature CPVs, 19/74, were stars with 2-minute TESS data acquired
 1724 between Sectors 1-55 that also met conditions 1-4. Our blind search (Table 1) recovered all but two of these 19 sources:
 1725 TIC 65347864 in Tuc-Hor (Popinchalk et al. 2023), and TIC 243499565 in Sco-Cen (Stauffer et al. 2021). During our blind
 1726 vetting, we manually labelled both sources as eclipsing binaries. Reconsidering with the knowledge of previous literature, we
 1727 believe that TIC 65347864 remains ambiguous: this source shows one persistent broad local minimum superposed over sinusoidal
 1728 spot modulation; it could be an eclipsing binary, an RS CVn, or a CPV.

1729 TIC 243499565 however is a bona fide CPV; our blind labeling for this source was incorrect. Stauffer et al. (2021) made the
 1730 classification based on Sector 11 full-frame image data. During Sector 38, the dip phases were different, and the source resembled
 1731 an eccentric eclipsing binary (similar to TIC 193831684). Sector 64 recently showed the development of additional local minima
 1732 in the light curve so that it shows three dips per cycle; its CPV classification is secure. Our search therefore missed one star that
 1733 had previously been classified as a CPV.

1734 *How many of our CPVs are new?*—Considering only our “good” CPVs, 35 of these 50 sources have not yet been reported
 1735 in the literature. Considering only the 13 “ambiguous” CPVs, 11 are new to the literature. Two sources, TIC 67897871

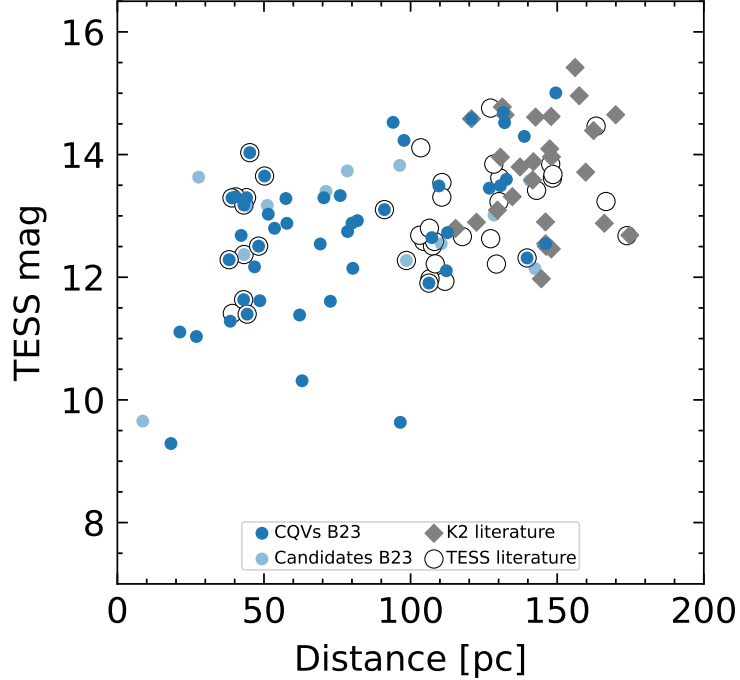


Figure 13. Brightnesses and distances of our CPVs compared against previous work. “K2 literature” corresponds to Stauffer et al. (2017) and Stauffer et al. (2018b). “TESS literature” corresponds to Zhan et al. (2019); Stauffer et al. (2021); Günther et al. (2022), and Popinchalk et al. (2023). “CQVs” and “candidates” are as in Figure 5, though for visual clarity unresolved binaries are not highlighted. PTFO 8-8695, a CPV at a distance of ≈ 350 pc, is not shown.

(EPIC 202724025; RIK-90; Stauffer et al. 2017) and TIC 118769116 (EPIC 247343526; Stauffer et al. 2017), were previously only known to be CPVs due to K2 observations. Both periods appear to have remained identical, within measurement precision. The shapes have of course changed. These two objects, combined with PTFO 8-8695, provide evidence that CPV variability persists over timescales of at least decades.

How do the brightness and distance distributions compare?—Figure 13 compares the TESS magnitudes and distances for the CPVs in Table 1 against the previously known literature CPVs. At the extremes, our new sources include the closest and brightest CPVs currently known. All K2 CPVs are in Sco-Cen, ≈ 100 -180 pc from the Sun. The large gap in the TESS literature CPV distance distribution was because the studies by (Zhan et al. 2019) and Popinchalk et al. (2023) both favored Tuc-Hor; many of our new CQVs are within this 40-100 pc gap.

D. NO SIGNIFICANT POWER AT 20 SECOND CADENCE

TESS was the first instrument to show that CPV light curves contain power at timescales of a few minutes (Zhan et al. 2019; Günther et al. 2022). This advance was enabled by the fifteen-fold faster cadence in the TESS 2-minute data, relative to K2. A logical follow-up is to ask whether the periodic components of the CPV light curves contain power at timescales below one minute. Between 2020 and 2021, we observed 10 CPVs at 20-second cadence with TESS in order to explore this question (TESS DDT029; PI L. Bouma). The stars were TICs 142173958, 146539195, 24518895, 276453848, 264599508, 363963079, 144486786, 408188366, 300651846, 262400835. These sources were selected from CPVs known at the time to have short periods and sharp features when observed at 2-minute cadence. Comparing the 20-second to 2-minute data for these stars (data available on MAST), we concluded that these CPVs did not contain appreciable power at timescales shorter than a few minutes, other than the usual flaring. This is consistent with the expected few-minute ingress and egress timescales for transiting circumstellar material.

E. THE CPVS ARE NOT OBVIOUSLY ACCRETING

We acquired iodine-free reconnaissance spectra using Keck/HIRES for three CPVs. The goals were to determine the chromospheric activity levels, and to check for indications of either accretion or spectroscopic binarity. We acquired a 15 minute exposure of TIC 146539195 on 2023 January 3, a 15 minute exposure of TIC 264599508 on 2023 January 9, and a 30 minute exposure of LP 12-502 (TIC 402980664) on 2023 July 10. The acquisition and analysis followed the usual techniques of the California Planet Survey (Howard et al. 2010). Figure 14 shows cutouts from the resulting spectra, centered on the Ca II HK windows, H α , and the

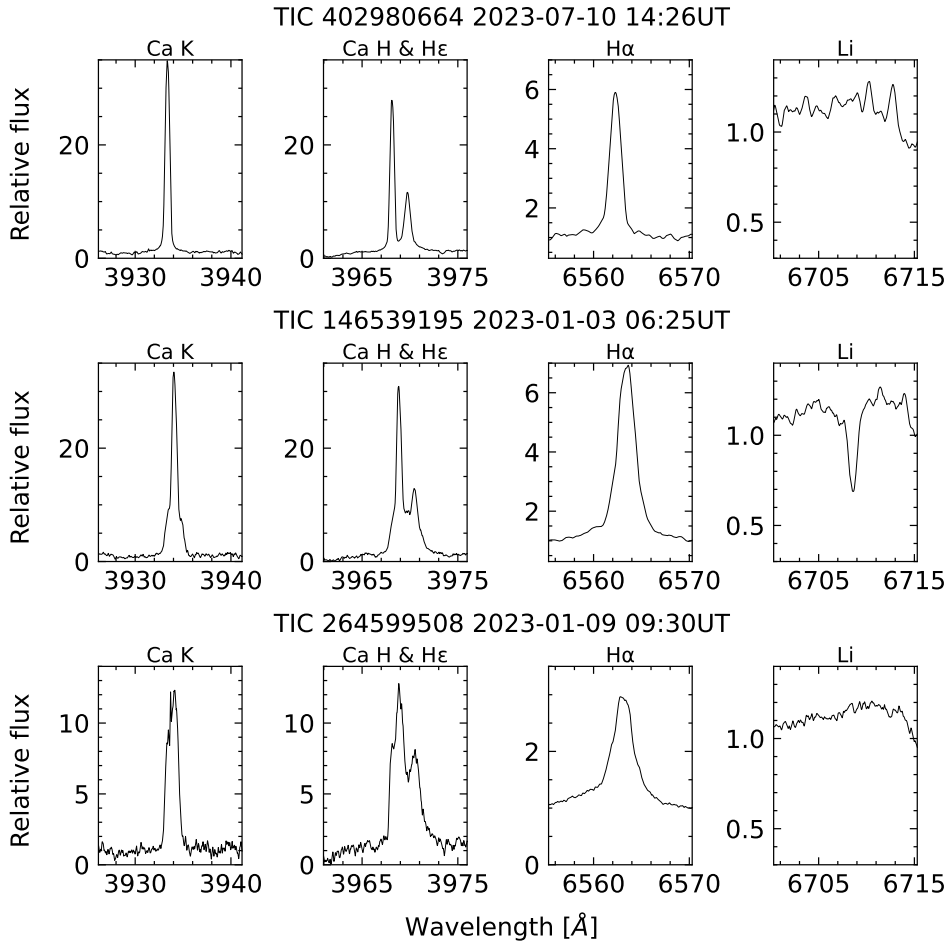


Figure 14. Spectral age and activity diagnostics for three CPVs. Wavelengths are in air; the continuum normalization is relative to the entire order. The $\text{H}\alpha$ emission strength classifies the stars as weak-lined T Tauris. The lithium detection for TIC 146539195 is consistent with its mass and β Pic membership; the non-detections for LP 12-502 (TIC 402980664) and TIC 264599508 are consistent with the ≈ 42 Myr age implied by their membership in the Columba moving group.

Li I 6708 Å doublet. The Ca II H emission line is blended with He ϵ . While a more detailed analysis will be left for future work, these spectra confirm previous understanding established by Stauffer et al. (2017) that the stars are chromospherically active M dwarfs in the “weak-lined” T Tauri regime (e.g. Briceño et al. 2019, Figure 15). Their $\text{H}\alpha$ equivalent widths, at ≈ 14 Å, ≈ 3 Å, and ≈ 8 Å (for TIC 264599508, 146539195, and 402980664 respectively) are consistent with purely chromospheric emission. The blue excess in TIC 264599508 could be explained by a second unresolved star; the TESS light curve for this source shows both the 7.90 hr CPV signal, and a 9.00 hr rotation signal with comparable amplitude.